Titre: Title:	Development of a Spatial Offset Raman Spectroscopy (SORS) Platform for Biological Tissue Interrogation
Auteur: Author:	Guillaume Sheehy
Date:	2018
Type:	Mémoire ou thèse / Dissertation or Thesis
Référence: Citation:	Sheehy, G. (2018). Development of a Spatial Offset Raman Spectroscopy (SORS) Platform for Biological Tissue Interrogation [Mémoire de maîtrise, École Polytechnique de Montréal]. PolyPublie. https://publications.polymtl.ca/3311/

UNIVERSITÉ DE MONTRÉAL

DEVELOPMENT OF A SPATIAL OFFSET RAMAN SPECTROSCOPY (SORS) PLATFORM FOR BIOLOGICAL TISSUE INTERROGATION

GUILLAUME SHEEHY
DÉPARTEMENT DE GÉNIE PHYSIQUE
ÉCOLE POLYTECHNIQUE DE MONTRÉAL

MÉMOIRE PRÉSENTÉ EN VUE DE L'OBTENTION
DU DIPLÔME DE MAÎTRISE ÈS SCIENCES APPLIQUÉES
(GÉNIE PHYSIQUE)
AOÛT 2018

UNIVERSITÉ DE MONTRÉAL

ÉCOLE POLYTECHNIQUE DE MONTRÉAL

Ce mémoire intitulé :

DEVELOPMENT OF A SPATIAL OFFSET RAMAN SPECTROSCOPY (SORS) PLATFORM FOR BIOLOGICAL TISSUE INTERROGATION

présenté par : SHEEHY Guillaume
en vue de l'obtention du diplôme de : Maîtrise ès sciences appliquées
a été dûment accepté par le jury d'examen constitué de :

M. GERVAIS Thomas, Ph. D., président
M. LEBLOND Frédéric, Ph. D., membre et directeur de recherche
M. PROVOST Jean, Ph. D., membre

DEDICATION

To my parents who always supported me,

To my brother,

To Catherine and our future ...

ACKNOWLEDGEMENTS

I would like to express my deep gratitude to my research supervisor Pr. Frérédic Leblond for his constant support, enthusiasm and for all the advice he gave me. He offered me a research internship four years ago, a scholarship three years ago and this project two years ago. I hope to continue working with him as it has been the most fulfilling experience I could have hoped for. He has a way to understand his students strengths and weaknesses that allows him to build a highly functional multidisciplinary team. I hope that our collaboration will continue.

I would like to thank all my colleagues, past and present, from the LRO and CRCHUM for their help. I would like to offer a special thank you to: Kelly Aubertin and Andrée-Anne Grosset who shared their knowledge and experience without reservation; Audrey Laurence, Karl St-Arnaud, Fabien Picot and Émile Beaulieu for their participation with the modern optics course; Frédérick Dallaire for his help and council during the redaction of this document; Arthur Poiffaut for his help with optical property measurements; and Layal Chaikho for all her work during the past three months and for all the data she acquired.

I would like to offer my thanks to the *Laboratoire de microfluidique pour l'oncologie* (muFO) and its students, most specifically to Amélie St-Georges-Robillard for her knowledge, experience and help with PDMS.

Finally, I would like to thank the members of the *département de génie physique de polytechnique montréal* most specifically Jean-Paul Lévesque and Yves Leblanc for their technical knowledge and experience, and Lyne Dénommé and Joanne Sirois for their constant and appreciated help.

RÉSUMÉ

La spectroscopie Raman (RS) devient un outil de plus en plus populaire pour le diagnostic du cancer. Mesurant la diffusion inélastique de la lumière associée aux modes de vibration des molécules, le signal Raman est spécifique à la composition moléculaire d'un échantillon. Lorsqu'il est mesuré sur un échantillon biologique, le signal Raman peut être utilisé pour la caractérisation et l'identification de celui-ci, et ainsi mener à un diagnostic. De plus, le signal Raman est entièrement intrinsèque et peut être couplé à un algorithme d'apprentissage automatique permettant la classification de tissus en temps réel. Au cours de la dernière décennie, une technique baptisée spectroscopie Raman à décalage spatial (SORS) a été utilisée afin d'augmenter la profondeur de pénétration du signal Raman dans les tissus biologiques.

Cependant, aucun modèle empirique n'a été établi permettant de relier le décalage spatial et la profondeur de pénétration pour une large gamme de propriétés optiques d'échantillons. De plus, l'effet de l'ouverture numérique (NA) des fibres optiques sur le signal SORS acquis reste inexploré. Ce projet consiste en la conception et la validation d'une plateforme de caractérisation SORS pour l'interrogation de tissus biologiques.

Tout d'abord, un système d'acquisition Raman existant a été optimisé et modernisé pour être utilisable avec une plate-forme de caractérisation SORS. En remplaçant les contrôleurs laser et en reprogrammant le logiciel d'acquisition, le contrôle de puissance laser a été amélioré et le temps d'acquisition a été réduit.

Deuxièmement, les outils logiciel de traitement et de classification des signaux Raman existants ont été mis à jour afin d'inclure des algorithmes d'extraction d'information et de permettre aux modèles de classification d'être exportés et validés sur de nouvelles données.

Enfin, une plate-forme de caractérisation SORS a été conçue et validée sur des fantômes optique nylon-PDMS à deux couches. En procédant à par enduction centrifuge du PDMS sur les disques de nylon, il a été possible d'obtenir de manière répétable une couche supérieure de 500 ± 50 μm de PDMS. Du TiO_2 a été ajouté au mélange de PDMS avant l'enduction ce qui a permis de modifier le coefficient de diffusion du PDMS. Les coefficients de diffusion des fantômes ont été mesurés de 0 cm^{-1} à 30 cm^{-1}.

ABSTRACT

Raman spectroscopy (RS) is becoming an increasingly popular tool for cancer diagnosis. Because RS measures inelastic light scattering based on the vibrational modes of molecules, Raman signal is specific to a sample's molecular composition. Thus, when performed on tissue, spectroscopic signal can be used for characterization and identification leading to a diagnosis. In addition, Raman signal is entirely label-free and can be coupled with machine learning algorithms for real-time tissue classification. In the past decade, a technique referred as Spatially Offset Raman Spectroscopy (SORS) has been used to increase the Raman signal penetration depth in biological tissue.

However, no empirical model has been established to link spatial offset and penetration depth for a large range of sample optical properties. In addition, the effects of the optical fibers numerical aperture (NA) on SORS acquired signals remains unexplored. This project presents the design and validation of a SORS characterization platform for biological tissue interrogation.

First, an existing Raman acquisition system has been optimized and modernized to be usable in conjunction with a SORS characterization platform. By replacing the laser controllers and by reprogramming the control software, the laser power control has been improved and the acquisition time has been reduced.

Then, existing Raman signal processing and classification toolboxes have been upgraded to include feature engineering algorithms and to allow trained classification models to be exported and cross validated on unseen data.

Finally, a SORS characterization platform has been designed and validated on two-layer nylon-PDMS based optical phantoms. By spin coating PDMS on nylon disks, it was possible to a uniform 500 ± 50 μm PDMS top layer. TiO_2 was added to the PDMS mix prior to spin coating to modify the PDMS diffusion coefficient. Phantoms diffusion coefficient were measured between 0 cm^{-1} to 30 cm^{-1}.

TABLE OF CONTENTS

LIST OF TABLES

LIST OF FIGURES

LIST OF SYMBOLS AND ABBREVIATIONS

ANN	Artificial Neural Network
CAD	Computer Assisted Design
CHUM	Centre hospitalier de l'Université de Montréal
CRCHUM	Centre de Recherche du CHUM
DAC	Digital-to-Analog Converter
FVB	Full Vertical Binning
GUI	Graphical User Interface
GUIDE	GUI Development Environment (*Matlab*)
kNN	k-Nearest Neighbor
LDA	Linear Discriminant Analysis
LRO	Laboratory of Radiological Optics
NA	Numerical Aperture
NEURO	Institut et hôpital neurologiques de Montréal
PCA	Principal Component Analysis
PLA	Polylactic Acid
QDA	Quadratic Discriminant Analysis
RS	Raman Spectroscopy
SBR	Signal to Background Ratio
SNR	Signal to Noise Ratio
SORS	Spatially Offset Raman Spectroscopy
SVM	Support Vector Machine

LIST OF APPENDICES

CHAPTER 1 INTRODUCTION

In 2015, it was estimated that 2 in 5 Canadians will develop cancer during their lifetime whereas 1 in 4 will die of cancer [2]. As the number of diagnosed cases increase, so does the need for improved disease detection techniques. For the past few years, optical spectroscopy and imaging technologies have seen steady increase in use due to their potential for minimally-invasive detection [3]. One of the main contender among these new optical techniques is Raman spectroscopy. By using an optical fiber probe and machine learning classification algorithms, Raman spectroscopy has reported high accuracy for the diagnosis of brain cancer [1, 3–5] and oral cancer [6, 7]. However, Raman spectra acquired with conventional probes are limited to the surface vicinity of probed samples.

In 2005, Spatially Offset Raman Spectroscopy (SORS) has been proposed as a simple approach to obtain spectral information from a sample subsurface layers [8, 9]. In the following years, more publications showed that the use of SORS could be extended to biological tissue [10–16] and for breast cancer diagnosis [17]. Although penetration depth of ~ 1 mm have been reliably achieved, no empirical relationship between spatial offset and penetration depth has been established. In summary, there is a need for a large scale study that investigates how the spatial offset affects the penetration depth of SORS signals and how it depends on the optical properties of the sample.

1.1 Hypotheses and objectives

This project was conducted within the Laboratory of Radiological Optics (LRO). The end goal consisted in the construction and validation of a SORS testing and characterization platform compatible with the existing LRO Raman acquisition system. However, it was established early on that the Raman system was in need of a systemic upgrade. At which point, three hypotheses were formulated,

1. The LRO's Raman system can be modified and optimized to reduce acquisition time, improve the signal to noise ratio (SNR) of acquired Raman spectra and limit wasted acquisitions during experiment sessions.

2. The LRO's Raman processing and classification toolboxes can be upgraded and standardized to improve classification performance, allow generalization of trained classification models, reduce overfitting and offer better visualization tools.

3. A SORS testing and characterization platform can be used to determine optimal fiber offsets for recovery of Raman signatures of deep layers in two layered optical phantoms.

Accordingly, the following objectives have been established,

1. Upgrade the LRO's Raman acquisition system.
   (a) Build new laser controllers to improve power control, stability and safety.
   (b) Modify the acquisition software to use the spectrometer's camera in a faster *acquisition mode*.
   (c) Reprogram the acquisition software in a language easier to maintain, upgrade and deploy than *LabView*.
   (d) Integrate live display of processed spectra to the software.
2. Standardize and upgrade the LRO's Raman processing and classification toolbox.
   (a) Implement an automatic cosmic ray removal algorithm.
   (b) Implement an automatic fluorescence removal algorithm.
   (c) Create a unified classifier training workflow
   (d) Rewrite the existing classification toolbox to export trained classification models and feature reduction matrix for generalization tests.
3. Build a SORS capable platform.
   (a) Build a SORS platform compatible with the existing Raman acquisition system
   (b) Design a SORS experiment on optical phantoms to characterize the effects of the spatial offset and the acquired Raman signal.

1.2 Organization of this document

This document consists of 6 chapters including the introduction. Chapter 2 presents a review of literature covering the current state of Raman spectroscopy, SORS and the use of machine learning for Raman spectra classification. Chapter 3, 4 and 5 cover the modernization of the LRO acquisition system, the development and standardization of the LRO signal processing and classification toolboxes and the development of a SORS characterization platform. Finally, chapter 6 concludes by synthesizing important results obtained and goals achieved during this project and by discussing future course of action and future research.

CHAPTER 2 REVIEW OF LITERATURE

This chapter consists of a brief overview of the current state of Raman Spectroscopy and its uses in medical applications, specifically cancer diagnosis. The first section will cover the basic concepts of Raman spectroscopy and the details on how it is performed on biological tissues. The second section covers Spatially Offset Raman Spectroscopy (SORS), a variation on the standard Raman spectroscopy technique that enables control on the probing depth for spectroscopic acquisitions. The third section will give the reader a basic understanding of classification techniques that can be used for tissue characterization using Raman spectroscopy.

2.1 Raman Spectroscopy

2.1.1 Raman scattering

Raman scattering, which was first observed by C.V. Raman and K.S. Krishnan in 1928 [18], is essentially an observation of inelastic scattering of photons traveling through a turbid medium. Suppose that a photon of frequency ω_0 and energy $E_0 = \hbar\omega_0$ is scattered by a molecule that possesses a vibrational mode of energy E_p. The photon interacts with the molecule by deforming the electron cloud surrounding it. It is absorbed and sends the molecule in a short-lived unstable state ($\sim$ 5 fs) [19]; a *virtual state*. The molecule rapidly radiates the excess energy and re-emits another photon in a random direction. Depending on the energy of the re-emitted photon, this process is refereed as either *Rayleigh*, *Stokes* or *Anti-Stokes* scattering (Figure 2.1).

In the case of *Rayleigh* scattering, which is much more likely, the scattered photon has the same energy as the incident photon. However, this photon does not carry vibrational information from the molecule it interacted with and as such will not be discussed further. On the other hand, for inelastic scattering, the scattered photon's energy changes according to the molecule's vibrational mode. Although *Stokes* and *Anti-Stokes* scattering probe the same information on the vibrational energy of the molecule, due to the small probability that a molecule is already in an exited vibrational state (such as S_{01} on Figure 2.1), *Anti-Stokes* scattering is much less likely to occur. At body temperature, since there is simply more molecules in the ground states than in a thermally excited state, *Stokes* scattering is simply more likely than *Anti-Stokes* scattering [20].

In addition to Raman scattering, other phenomena can occur when light interacts with

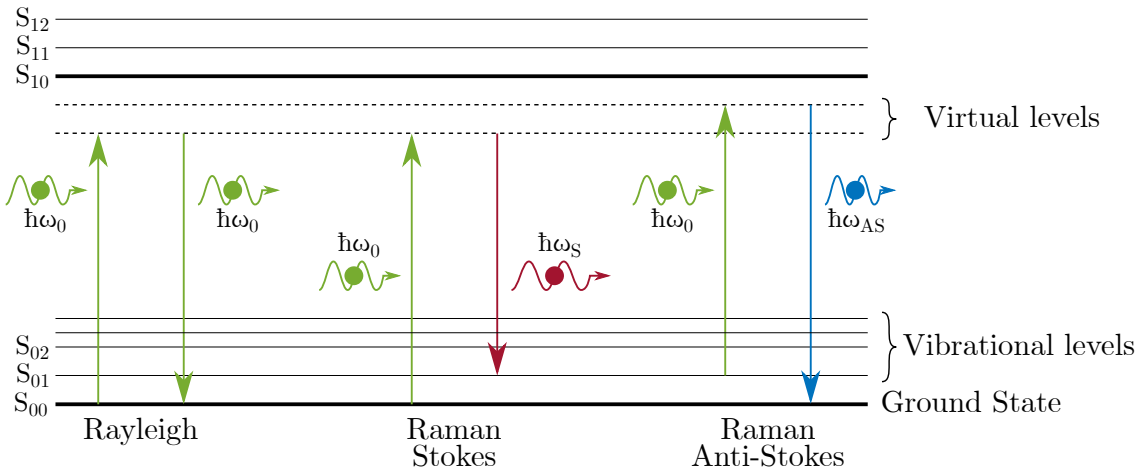

Figure 2.1 Jablonski diagram of possible scattering interactions.

matter. Specular reflection, absorption and fluorescence are all competing processes that can hinder our ability to detect the Raman signal from samples. Tissue fluorescence signals are typically $2-5$ times greater than Raman signal and Rayleigh scattering can be up to several orders of magnitude greater than Raman scattering. It then becomes necessary to use high power lasers as excitation source and filter out the excitation wavelength before detection. Details on acquisition systems and signal processing will be covered in later sections.

For Raman *Stokes* scattering, $E_S = \hbar\omega_0 - E_p$. The molecule's vibration energy is written

$$E_p = \hbar\left(\omega_0 - \omega_S\right), \tag{2.1}$$

or more conveniently

$$E_p = hc\left(\frac{1}{\lambda_0} - \frac{1}{\lambda_S}\right) = hc\Delta\omega. \tag{2.2}$$

where λ_0 is the wavelength of the incoming photon and λ_S is the re-emitted *Stokes* photon. Since the energy involved in vibrational state transitions is generally small (< 500 meV), a common practice in spectroscopy is to use a photon wavenumber instead of its energy (Figure 2.2). With Raman spectroscopy the Raman shift $\Delta\omega$ in cm^{-1} is used to quantify energy,

$$\Delta\omega[\text{cm}^{-1}] = 10^7\left(\frac{1}{\lambda_0[\text{nm}]} - \frac{1}{\lambda_S[\text{nm}]}\right), \tag{2.3}$$

A direct and very important consequence of equation 2.3 is that in order to acquire a high

resolution Raman spectrum, it is critical to use a monochromatic excitation source. The broader the excitation source is the broader the acquired Raman peaks will be. Thus, Raman excitation sources must be narrow ($FWHM < 3$ nm) and its emission wavelength and power must be stable over time.

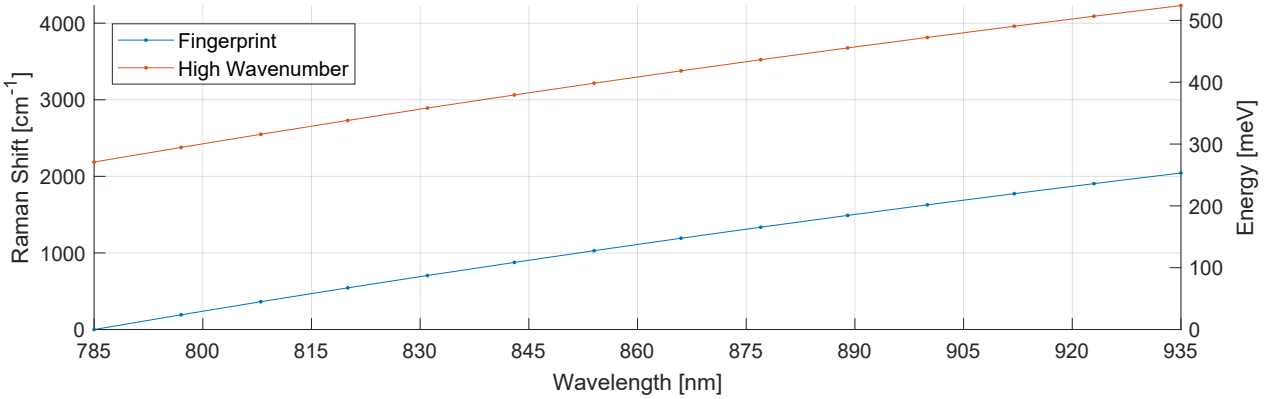

Figure 2.2 Relationship between a photon's wavelength, Raman Shift and energy for *fingerprint* ($\lambda_0 = 785$ nm) and *high wavenumber* $\lambda_0 = 670$ nm regions.

Hence, Raman *Stokes* scattering can be used to measure the vibrational energy levels of a molecule. It however remains an inherently weak process in comparison to *Rayleigh* scattering. In practice, only about 1 in $10^6 - 10^8$ photons will undergo inelastic scattering. Thus, the use of a high power density source such as a laser is required in order to generate a sufficiently high Raman signal. The use of lasers also dramatically increases the amount of Rayleigh scattered photons. It is then necessary to filter the Rayleigh scattered light with a high pass filter centered at the laser's wavelength before reaching the spectrometer. When using a laser as a pump in conjunction with a filter before detection, it becomes possible to acquire the Raman spectrum of a sample.

Common drugs such as *acetaminophen* and *ibuprofen* are used as benchmarks to calibrate Raman acquisition systems (Figure 2.3). Each peak represents a vibrational transition of the molecules present in the sample. The Raman spectrum region from 0 to 2000 cm^{-1} is refereed to as the *fingerprint* region and the region from 2000 cm^{-1} to 4000 cm^{-1} is called the *High Wavenumber* region. Several organic molecule have vibrational modes such as C–C, C=C, C–N and C=O stretching in the *fingerprint* region and CH=CH, C-CH3, O-H stretching in the high *wavenumber* region [20,21]. Due to its high chemical specificity, Raman spectroscopy has been proven to be a useful tool for sample identification and characterization in the mining industry [22] and the pharmaceutical industry [23].

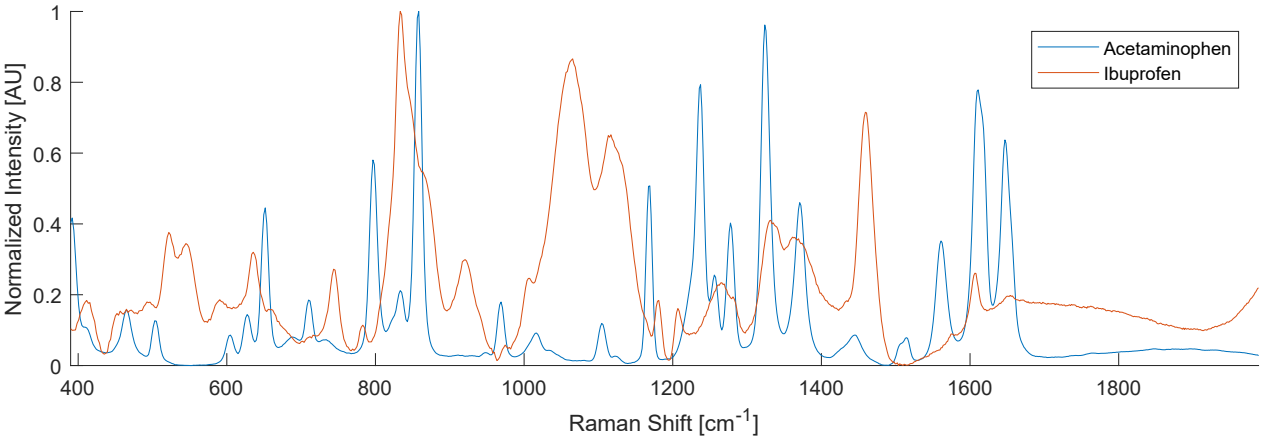

Figure 2.3 Normalized Raman spectra of *acetaminophen* and *ibuprofen* in powder form. The spectra were acquired with the Raman system presented in chapter 3.

2.1.2 Tissue fluorescence and SNR

Compared to organic minerals and single molecule compounds, Raman spectroscopy performed on biological samples such as tissues is much more difficult. Because a biological samples consists of a large amount of different types of molecules each with it's own unique Raman fingerprint, its Raman signal is much less intense and has a significantly lower signal to noise ratio (SNR). In addition, autofluorescence from biological samples is generally much greater than for non-biological samples (Figure 2.4) which also lowers the signal to background ratio (SNB) of the Raman peaks.

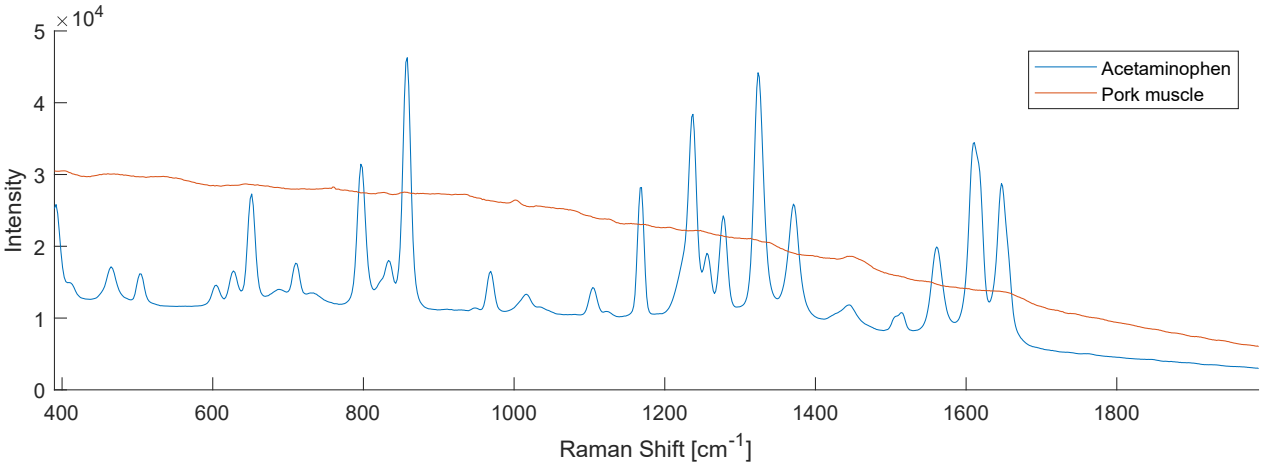

Figure 2.4 Raw Raman signal from *acetaminophen* in comparison to pork muscle tissue. Acquisition was performed with the Raman system presented in chapter 3.

In order to remove the contribution of autofluorescence from the Raman signal, a polynomial fitting procedure can be used. The auto-fluorescence profile can be approximated by a polynomial function but there is no consensus in the field on the best polynomial fit order [24]. Moreover, one cannot simply use polynomial fitting over the raw Raman data without risking the removal of important Raman bands which is critical to avoid. It is necessary to use an iterative algorithm that first identifies the Raman peaks and removes them before attempting to fit the polynomial function on the autofluorescence signal alone.

2.1.3 Raman spectroscopy for cancer diagnosis

Tissue characterization at the molecular level could prove useful for cancer diagnosis [4]. As tissues are becoming cancerous, the very delicate balance of biochemical processes normally occurring within healthy cells changes [25]. These slight changes in biochemistry can be used as a intrinsic cancer biomarker that can be detected and quantified with Raman spectroscopy. Following improvements made on instrumentation and raman signal processing techniques during the last decade, Raman spectroscopy has been established as a potential tool for real time diagnosis of cancer [1, 3–5].

Typical Raman acquisition systems consist of a laser, a spectrometer, a camera and an optical instrument. The acquisition instrument can be a front viewing optical fiber probe [1], a side viewing modified biopsy needle [5] or even a microscope [26]. Raman microscopes allow for fast acquisition of multiple spectra used for building statistical models and machine learning classification algorithms whereas optical probes can easily be used by surgeons or clinicians for real time tissue diagnosis. Additionally, since the Raman signal is intrinsic to the molecules already present in tissues, there is no need to inject additional biomarkers, such as fluorophores, that would be necessary for other spectroscopy techniques [4].Hence, the minimally invasive and highly specific character, as well as the low cost of Raman spectroscopy makes it potential diagnostic tool for cancer. Nonetheless, to be truly usable for real time diagnosis, Raman spectroscopy needs to be coupled with an automated classification algorithm such as a support vector machine (Section 2.3).

2.1.4 Challenges in Raman spectroscopy : problems and solutions

As mentioned in the previous sections, Raman spectroscopy can be a powerful tool for biological characterization. However, the following problems need to be addressed in order to acquire Raman spectra that can be distinguished from other less subtle background contributions:

1. Intrinsic tissue absorption can dramatically reduce the intensity of the signal.
2. Rayleigh scattering is orders of magnitude (at least $3-6$) larger than Raman scattering, which often lead to filter bleed-through that reduces the detector dynamic range.
3. Fluorescence signal is several times ($\sim 20\times$) bigger than Raman signal on biological tissues.

Fortunately, the following solutions can help alleviate these problems

1. The laser wavelength can be chosen to maximize Raman signal ($I_{Raman} \propto 1/\lambda_0^4$), minimize fluorescence ($I_{Fluo} \propto 1/\lambda_0$) and avoid the main tissue absorption band.
2. Laser power and exposure time can be fine-tuned to maximize utilization of the full dynamic range of spectrometers while staying below safe light exposure levels.
3. Narrow bandpass (sometime called *laser line*) filters can be used to assure narrow band excitation to minimize filter bleed through.
4. High pass filters with cut-off slightly below the excitation wavelength can be used in front of the spectrometer to further limit Rayleigh scattered light bleed-through and avoid detector saturation.

Depending on the application, some or all of these solutions may be used.

Since no Raman microscopes were used in this project, they will not be discussed. However, a Raman fiber optics probe manufactured by *EmVision LLC* (FL, USA) was used as a validation tool for the Raman system presented in chapter 3. This type of probe has already been shown to be effective for accurate detection of brain cancer [1]. The probe has a single centered fiber for laser excitation and 8 collection fibers surrounding it. Two filters are placed after the probe's fibers. The center filter is a low-pass filter at $\lambda < 785$ nm that allows tissue excitation for both fingerprint ($\lambda_0 = 785$ nm) and high wavenumber ($\lambda_0 = 670$ nm) acquisitions. The outer (donut-shaped) filter is a high-pass filter at $\lambda > 785$ nm that blocks Rayleigh scattered light from the sample. A focusing lens placed at the distal end to overlap the excitation and collection light cone. This design can be used for *conventional Raman spectroscopy* where the excitation and collection are done at the same site ($radius < 500$ μm).

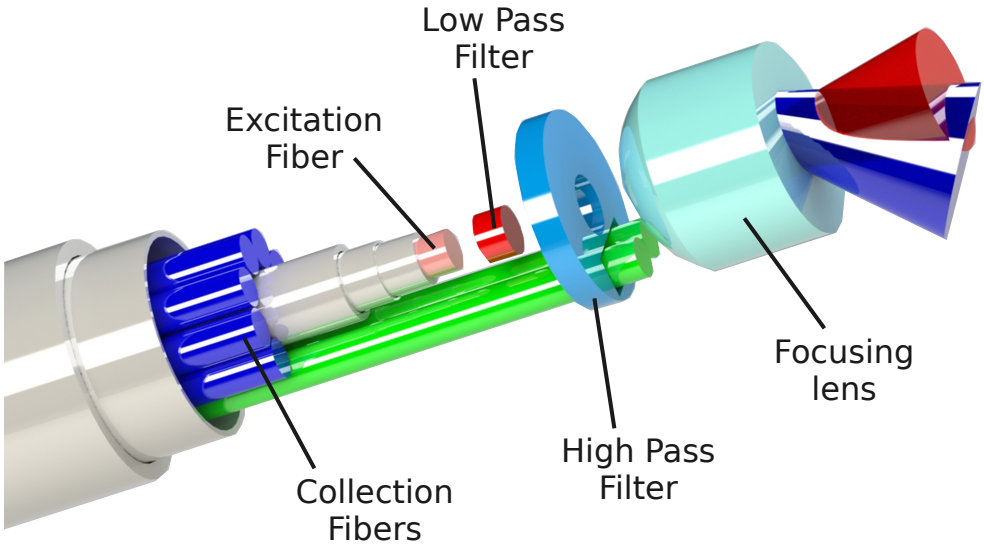

Figure 2.5 Commercial Raman probe used for validation of Raman System presented in chapter 3 (Adapted from [1]).

2.2 Spatially Offset Raman Spectroscopy (SORS)

Conventional Raman spectroscopy can provide specific information from the surface of a sample, but it is very limited in penetration depth. In 2005, Pavel Matousek proposed a simple technique that can extend the use of conventional Raman spectroscopy to the imaging of deeper layers ($\sim$ 1 mm) in a sample [8, 9]. The technique was then christened Spatially Offset Raman Spectroscopy (SORS). SORS has been shown to be a simple and effective technique to retrieve the Raman spectrum of the sublayer in a two-layer tissue mimicking optical phantoms. The technique exploits photon diffusion in a scattering (turbid) medium. Briefly, two fibers are used; one for excitation with laser light, the other for collection of spectroscopic data. The collection fiber is laterally offsetted by Δs from the excitation fiber (Figure 2.6). By increasing the Δs, the path (banana) taken by the collected photons is pushed deeper into the sample [17].

To characterize the effect of the spatial offset on the collected signal and the shape of the diffusion banana, it is useful to define the SORS ratio as a function of Δs

$$SORS_{ratio}(\Delta s) := average_{\lambda}\left(\left[\frac{I^{b}_{\lambda}(\Delta s)}{I^{t}_{\lambda}(\Delta s)}\right] / \left[\frac{I^{b}_{\lambda}(0)}{I^{t}_{\lambda}(0)}\right]\right), \tag{2.4}$$

where $I^{b}_{\lambda}(\Delta s)$ and $I^{t}_{\lambda}(\Delta s)$ are the intensity of the most prominent Raman peaks emitted from the bottom and top layer in function of Δs and $I^{b}_{\lambda}(0)$ and $I^{t}_{\lambda}(0)$ are the intensity of the most

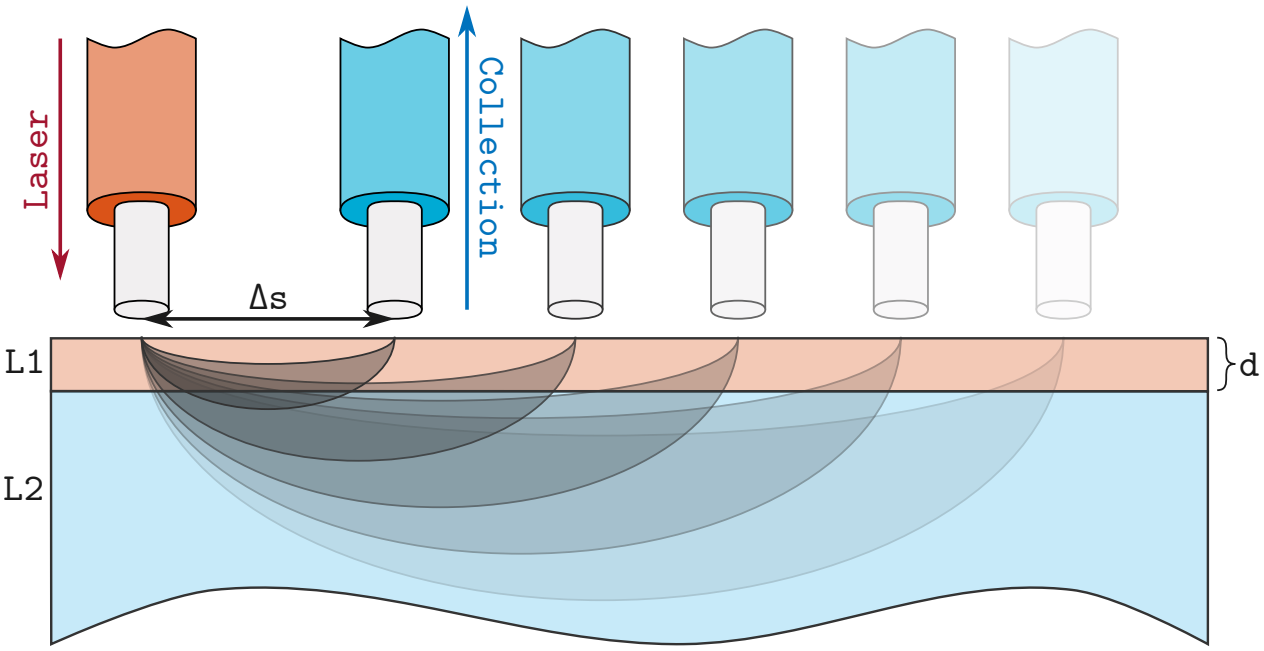

Figure 2.6 Schematic of a SORS measurement with a spatial offset Δs and a surface layer of thickness d.

prominent Raman peaks emitted from the bottom and top layer when $\Delta s = 0$.

The technique has already been described with Monte Carlo models [9] and experiments [8] and been demonstrated for in vivo human tissue spectroscopy [10]. Penetration depth of 1 mm have been reported on two layers optical phantoms (Aquisition time = 100 sec/spectrum, laser power = 12.5 mW) [12]. More recently, penetration depth of up to $\sim$ 2 mm have been achieved within breast tissue (Aquisition time = 20 sec/spectrum, laser power = 80 mW) [17]. In general,

1. the SORS ratio increases with Δs;
2. the SORS ratio is independent of the top layer thickness (d);
3. the technique's usability is only limited by the availability of Raman signal from the bottom layer;
4. the technique can be used to recover nearly pure spectra from the bottom layer (spectra exempt from top layer Raman signature) without prior information of the top layer composition ($I^t_\lambda(\Delta s) \propto 1/SORS_{ratio}(\Delta s)$);
5. with proper information on both layer's composition, the technique can be used for tumor margin assessment [14].

Although promising, performing SORS on biological tissue is difficult. The overall Raman signal from the sample diminishes when increasing the spatial offset, which reduces the SNR (SNR $\propto 1/\Delta s$). The choice of Δs for specific applications remains a trial and error process of optimization of the tradeoff between the penetration depth ($\propto \Delta s$) and the Raman signal intensity (SNR).

2.3 Machine Learning and Classification

Machine learning refers to a subset of techniques from the artificial intelligence field of computer science. It is based on computational statistics and mathematical optimization. Evolving from pattern recognition, machine learning techniques are used for data prediction, automated decision making, anomaly detection and more. Most common and well known machine learning applications include email filtering (spam detection), optical character recognition, recommendation systems (such as *YouTube*'s *Recommended* videos) and self driving cars. Typical machine learning problems can be categorized either as 'supervised learning' or 'unsupervised learning'. In 'supervised learning' problems, algorithms are "trained" with prelabeled data. A common example would be to train a system to identify pictures of cats and dogs by training it with a set of pictures pre-labeled 'Cat' or 'Dog'. In 'unsupervised learning', algorithms are "trained" without data labels and are generally used for clusterization and dimensionality reduction of a dataset.

2.3.1 Classification of Raman spectra

In order to extend the use of Raman spectroscopy to clinical applications, an automated classification algorithm is required for spectrum assessment and diagnosis. Statistical models and machine learning algorithms can be used for automated real-time classification of Raman spectra acquired on unknown tissue. Many different classification algorithms have successfully been used for automatic labeling of a sample as 'Cancerous' or 'Benign'. Table 2.1 presents some of the successful results other groups had with Artificial Neural Networks (ANN), k-Nearest Neighbors (kNN), Discriminant Analysis (LDA or QDA), Principal Component Analysis (PCA) and Support Vector Machine (SVM). Although some algorithms seem to yield excellent results, no consensus has been reached as to which algorithm performs best in general. Choosing the best classifier and training parameters for a specific pathology is a tedious process of testing and optimization. Fortunately, testing algorithms on specific datasets can easily be done with existing machine learning toolboxes implemented for high level programming languages such as *Matlab* or *Python*. As SVM classifiers are becoming more and more frequent, are very reliable in producing good results and are easy to interpret,

it is the only classifier discussed further in this work.

Table 2.1 Overview of classification techniques results for raman spectroscopy based cancer detection in the literature. Accuracy, sensitivity and specificity are computed by comparing trained classifier prediction to histopathological results (gold standard).

Cancer type	Instrument	Classification Problem	Model	Accuracy	Sensitivity	Specificity
Skin cancer [27]	handheld spectroscope	malignant vs healthy	ANN	96%	94%	99%
Brest cancer [28]	optical probe	cancerous vs normal	kNN	89%	93%	78%
Gastric cancer [29]	optical probe	dysplasia vs normal	LDA	92%	95%	90%
Gastric adenocarcinoma [30]	microscope	adenocarcinoma vs normal	LDA	98%	98%	100%
Gastric cancer [31]	free space system	carcinoma vs normal	PCA	70%	66%	73%
neuroblastoma, cervical, ovarian,... [32]	microscope	one vs all	QDA	100%	100%	100%
Breast cancer [33]	microscope	cancerous vs normal	SVM	up to 100%	up to 100%	up to 100%

2.3.2 Support Vector Machine

The Support Vector Machine algorithm works by finding a *decision boundary* (frontier) within the *feature space* of the data. The *feature space* simply refers to the n-dimensions space where each data points lives. For Raman spectra, each *feature* (F_i) of the space corresponds to the intensity $I(RS_i)$ measured for the Raman Shift RS_i [cm^{-1}]. In that space, each Raman spectra can be represented as a single point or vector and the *decision boundary* segregates Raman spectra belonging to a class from another. In order to understand how the decision boundary is decided, it is useful to first understand what "support vectors" are. A support vector is a data point of a given class that is closest to the opposing class. In order to find the best decision boundary, the algorithm looks at the support vectors and finds the line (hyperplane) that maximizes the total distance between the decision boundary and the support vectors. Hence, SVM models are often referred to as 'large margin classifiers'. Figure 2.7 illustrates how a linear SVM model behaves when trained on a binary classification problem (2 classes) with a 2-dimensional dataset (for visualization). It becomes easy to see how the decision boundary chosen maximizes the area between the margins and how both margins are enclosed by support vectors. For higher dimensions, the decision boundary becomes a plane (or hyperplane).

SVM classifiers can also be used to classify data that are not linearly separable. A *kernel function* (sometimes refereed as the *kernel trick*) can be used to express data in a new dimensional space in which it becomes linearly separable [34] (Figure 2.8). Most common kernels include the linear kernel (eq. 2.5), the polynomial kernel (eq. 2.6) and the Gaussian

radial basis function (eq. 2.7).

$$K(\vec{x_i}, \vec{x_j}) = \vec{x_i} \cdot \vec{x_j} + 1 \tag{2.5}$$

$$K(\vec{x_i}, \vec{x_j}) = (\vec{x_i} \cdot \vec{x_j} + 1)^d \tag{2.6}$$

$$K(\vec{x_i}, \vec{x_j}) = exp\left\{\frac{-||\vec{x_i} - \vec{x_j}||^2}{2\sigma^2}\right\} \tag{2.7}$$

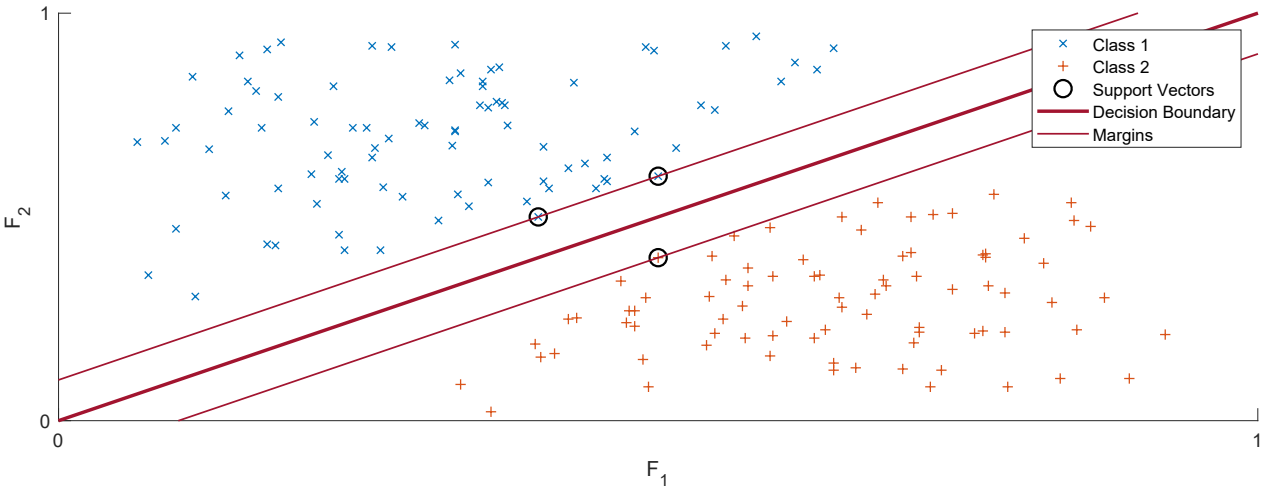

Figure 2.7 Illustration of an SVM boundary decision, margins and support vector for a binary classification problem in 2d.

2.3.3 Underfitting and overfitting

Overfitting and underfitting are common terms used in machine learning to qualify how a model might fit a dataset. Underfitting occurs when a statistical model or a classification algorithm fails to properly capture the underlying trend of the data (Figure 2.9a). This generally happens when the model used is too simple, has a high bias and low variance or when data is represented with not enough features (variables). On the other hand, overfitting occurs when a statistical model or a classification algorithm captures the noise of the data (Figure 2.9c). This can happen when the model used is too complex, has a low bias and high variance, when data is represented with too many features or when the number of parameters in the classification model is comparable to the number of data used for training. Both overfitting and underfitting models will result in poor a classification performance on

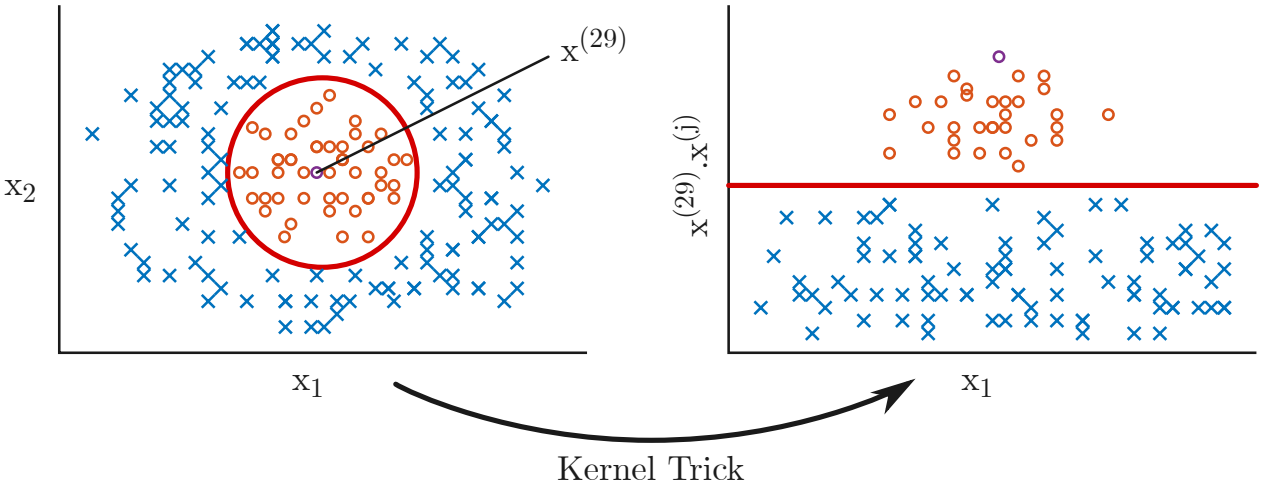

Figure 2.8 Illustration of the kernel trick basis transformation.

unseen data. As per the goldilock principle (not too much, not too little), the best model is the one that fits the data just right (Figure 2.9b).

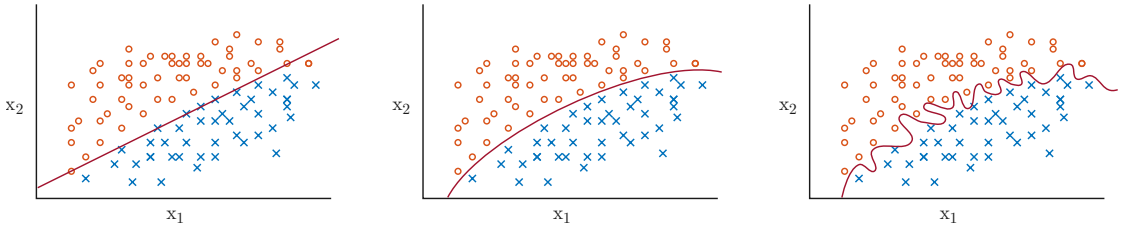

(a) Underfitting (b) Appropriate fitting (c) Overfitting

Figure 2.9 Illustration of the three possible model fitting outcomes.

2.3.4 Quantifying performance

Although simple and easy to compute and understand, accuracy [%] generally makes for a poor performance metric to quantify how well a classifier performs. For instance, when the different classes present in a dataset are unbalanced (not 1:1), the following situation can occur. Picture a dataset comprised of 100 spectra; 95 spectra of healthy tissue, 5 spectra of cancerous tissue. A classifier that always outputs "healthy" as a prediction will get an accuracy of 95% on the dataset, while in reality, it performed poorly. A better performance metric is the Receiver Operating Characteristic (ROC) curve and the area under the curve (AUC) [35].

ROC curves are graphical plots that illustrates the performance of a binary classification model. By translating the boundary decision of a classifier, it is possible to plot the true positive rate as a function of the false positive rate. When represented in the ROC space, a perfect classifier corresponds to the point $(0, 1)$ while a random guess corresponds to any point along the line between $(0, 0)$ and $(1, 1)$. Every possible model can be represented by a ROC curve between a random guess and a perfect classifier (Figure 2.10). The AUC under the ROC curve can be used to quantify the performance of a classifier. A random guess has an AUC $= 0.5$, a perfect classifier has an AUC $= 1$ and every possible classifier has an AUC $\in [0.5, 1]$. A larger AUC means a better classifier.

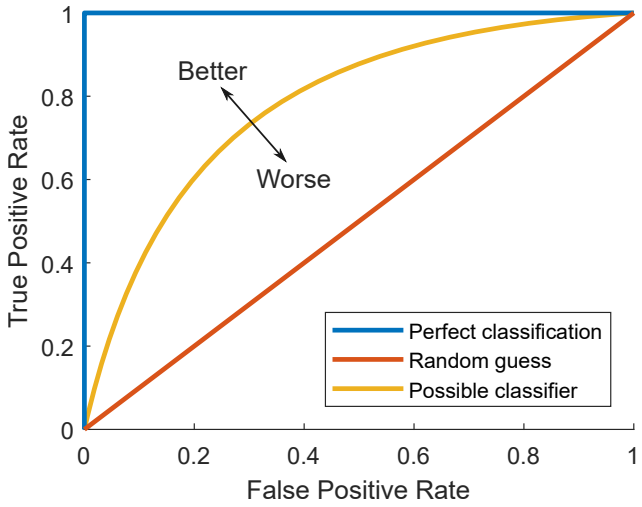

Figure 2.10 Illustration of a perfect classification model, possible classifier and random guess ROC curves.

CHAPTER 3 RAMAN AQUISITION SYSTEM

This chapter covers the modernization and optimization of the two *Laboratory of Radiological Optics*'s (LRO) Raman acquisition systems. The first section covers the modernization process and the technical details. The second section covers the results and validation of the final system.

3.1 Modernization and optimization

After a preliminary testing phase, it was decided that the following problems needed to be addressed.

1. Laser power control inputs from the user were utilized by the software without prior laser calibration through the connected optical instrument. This issue resulted in unstable and potentially damaging levels of exposure for the samples. Also, since the actual power delivered during an acquisition was unknown, laser power parameters could not be used for spectra processing or analysis.

2. The spectrometer's camera was used in a suboptimal *acquisition mode*. This led to unnecessarily long acquisitions, during which samples would be needlessly exposed to high laser power.

3. The previous acquisition software was programmed with the *LabView* system-design platform. This unfortunately caused the software to be unreliable as well as difficult to modify, upgrade and maintain.

4. Only raw spectra were displayed on the Graphical User Interface (GUI) during acquisition. This made it nearly impossible for real time quality assessment. Spectra would often be unusable because of low Raman signal unbeknownst to the user.

Additionally, both Raman systems (Figure 3.1) owned by the LRO did not use the same acquisition software. Although not a priority, compatibility of the acquisition software to both current and future systems would allow easier comparison between spectra for different studies and a unified processing workflow.

The first Raman system is generally used at the *Institut et hôpital neurologiques de Montréal* (NEURO). This system uses a 671 nm laser from *Laser Quantum* for high wavenumber

Raman acquisition and a 785 nm laser from *Innovative Photonic Solutions* for *fingerprint* acquisition. The spectrometer and camera package were manufactured by *EmVision* and use *Andor Newton 920* cameras.

The second Raman system (Figure 3.2) generally stays at the *Centre de recherche du Centre hospitalier de l'Université de Montréal* (CRCHUM). This system uses a dual 670-785 nm wavelength laser from *Innovative Photonic Solutions* for both high wavenumber and fingerprint Raman acquisition. The spectrometer and camera package is the same as for the NEURO system.

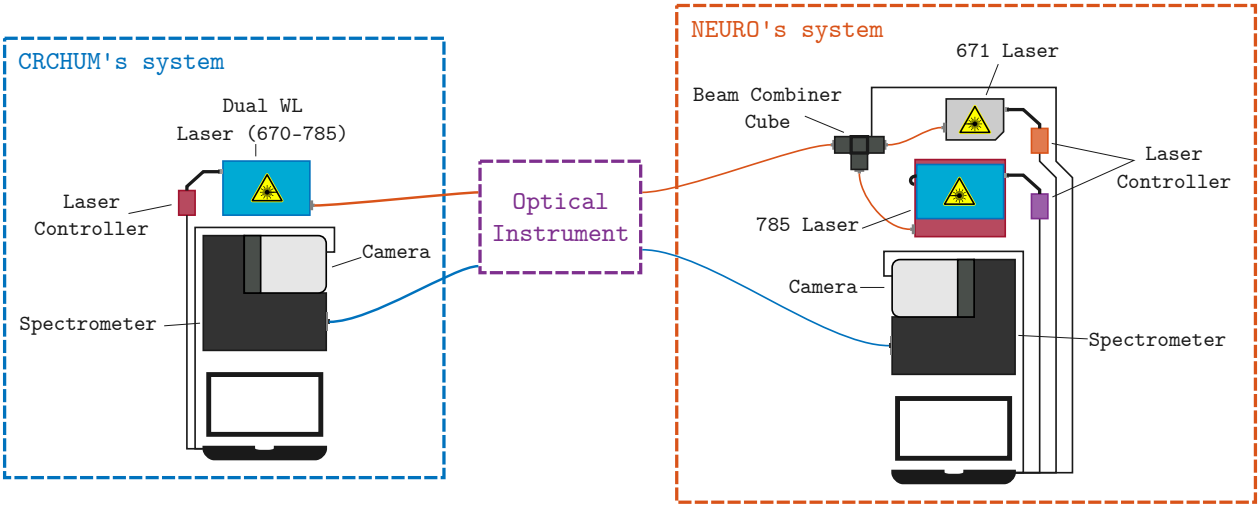

Figure 3.1 Hardware schematic of the upgraded LRO Raman acquisition systems.

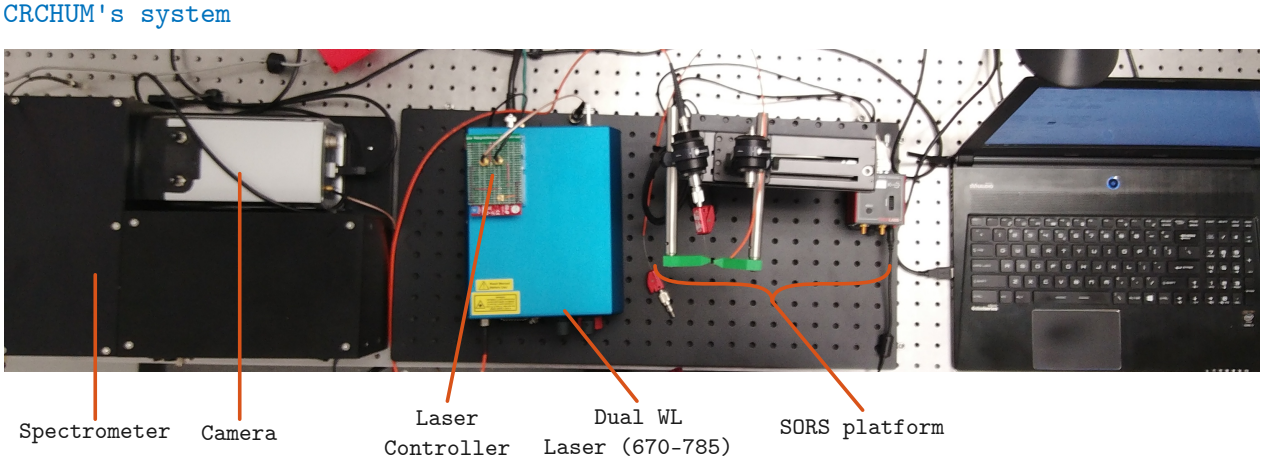

Figure 3.2 Picture of CRCHUM's Raman system.

3.1.1 Laser control

The first step in the modernization of the Raman acquisition systems was to solve the issues with laser power control. In order to solve the laser calibration and stability issue, new laser controllers were built to replace the ones provided by the different laser manufacturers.

Both IPS's lasers are controlled via an analog voltage input to a female BNC port at the back of the laser. The BNC voltage input [0 to 2.5 V] is mapped to the laser power output [0 to P_{Max} mW]. Both controllers are based on an *Arduino* microcontroller connected to a *SparkFun* digital-to-analog converter (DAC). A code allowing the acquisition software to send commands to the controllers was written, compiled and embedded on the arduino. Then, the acquisition software sends a command to the laser controller via a *serial* communication USB port. By sending the command "(V, T)" as a string to the microcontroller, the laser will turn on with a power $P = k \cdot V \ mW$ for $T \ ms$. In order to determine a value for k [mW/mV], a laser calibrations procedure must be run by the software prior to a Raman experiment (section 3.2.1). The complete *IPS* laser controller circuit schematic is presented in Appendix A.

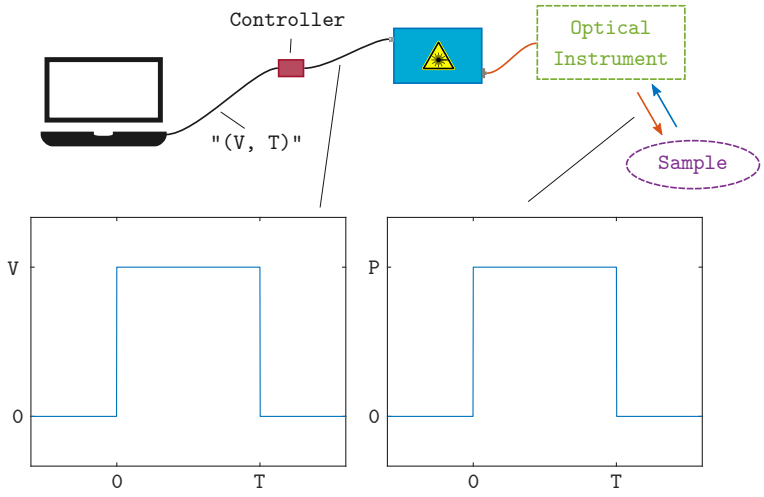

Figure 3.3 Operation illustration of the *IPS* laser controllers.

The *Laser Quantum* laser had an additional issue that needed to be solved. This laser has a very long stabilization time of about one minute which is problematic since Raman acquisitions typically take less than a few seconds. Average intensity of spectra acquired during the same acquisition fluctuates following variations in laser power (Figure 3.4). To solve this issue, a mechanical shutter (*Thorlabs* SHB05T) was installed in the beam combiner cube (Figure 3.5). This allowed the user to set the laser to the desired power and wait for

it to stabilize ($\sim 1-2$ minutes) before starting an acquisition. The replacement controller has been designed to control both the laser and the mechanical shutter. This laser uses an *RS232* serial communication protocol instead of a simple BNC analog input. Instead of a DAC shield, the controller for this laser uses an *arduino* with an RS232 shifter shield (*SparkFun RS232 Shifter - SMD*). The arduino relays the serial command strings from the computer to the shifter shield which then converts the arduino's TTL serial signal to RS232 for the laser. The arduino also controls the mechanical shutter via a digital voltage to the shutter's external control's BNC input ($0V \rightarrow Close$, $5V \rightarrow Open$). The complete *Laser Quantum* laser controller circuit schematic is presented in Appendix B.

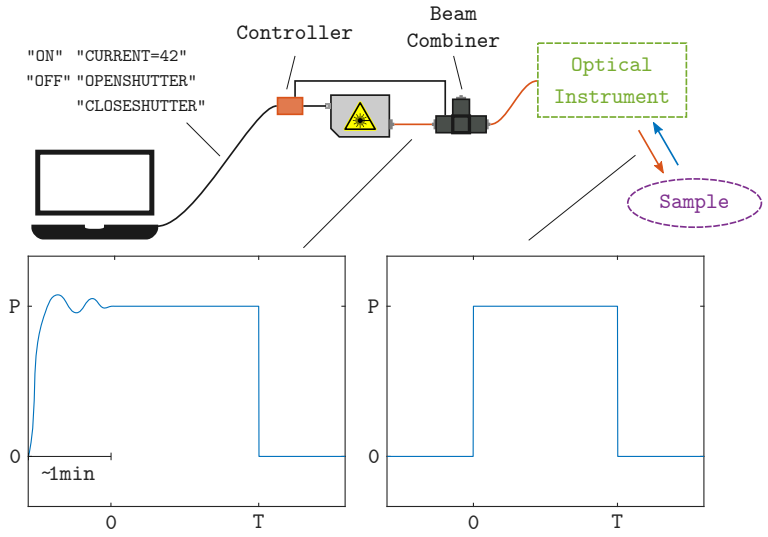

Figure 3.4 Operation illustration of the *Laser Quantum* laser controller.

With the safer and improved controllers, it is now possible to set a specific excitation laser power for Raman acquisitions. However as for the IPS laser, the user must perform a laser calibration curve measurement with the software (see section 3.2.1) prior to each experiment. Doing so allows the system to account for the different light loss that occur in the optical instrument. Calibration curves are also a powerful tool that facilitates system issue diagnosis and maintenance.

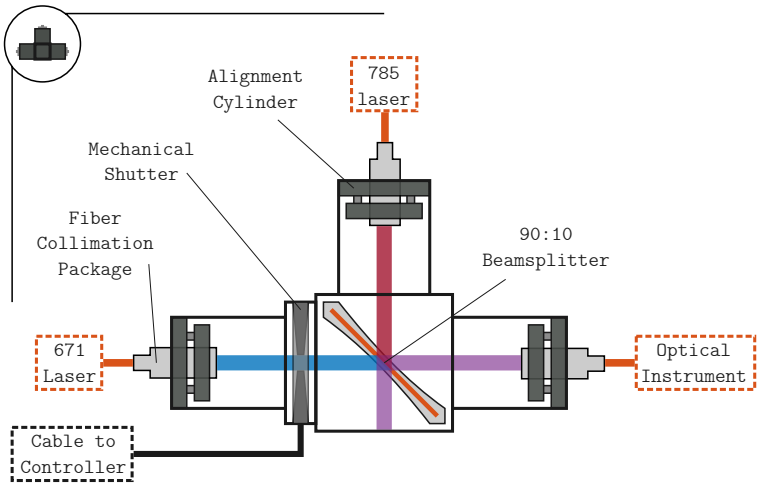

Figure 3.5 CRCHUM system beam combiner schematic.

3.1.2 Spectrometer and camera

Both LRO's Raman systems use a spectrometer and camera package manufactured by *EmVision* based on *Andor Newton 920* cameras. *Andor Newton 920* cameras use a Charged Coupled Device (CCD) detector divided as a 2-dimensional (1024x255) array of pixels. In order to use the camera as a spectrometer sensor for Raman acquisitions, parameters given in Table 3.1 are used by the acquisition software.

Table 3.1 Camera parameters used by the acquisition software.

Parameter	Value
Readout mode	Full Vertical Binning (FVB)
Acquisition mode	Kinetic Series
Trigger mode	Internal
Shutter mode	Open during FVB series
Cooling temperature	$-70°C$

Readout mode refers to the different ways that the camera chip can be spatially binned during reading. Since the spectrometer's grating is oriented so that wavelengths are separated along the horizontal axis of the sensor and fibers are aligned along the vertical axis, the best **readout mode** for spectroscopic application is the **Full Vertical Binning** (**FVB**) mode illustrated in Figure 3.6.

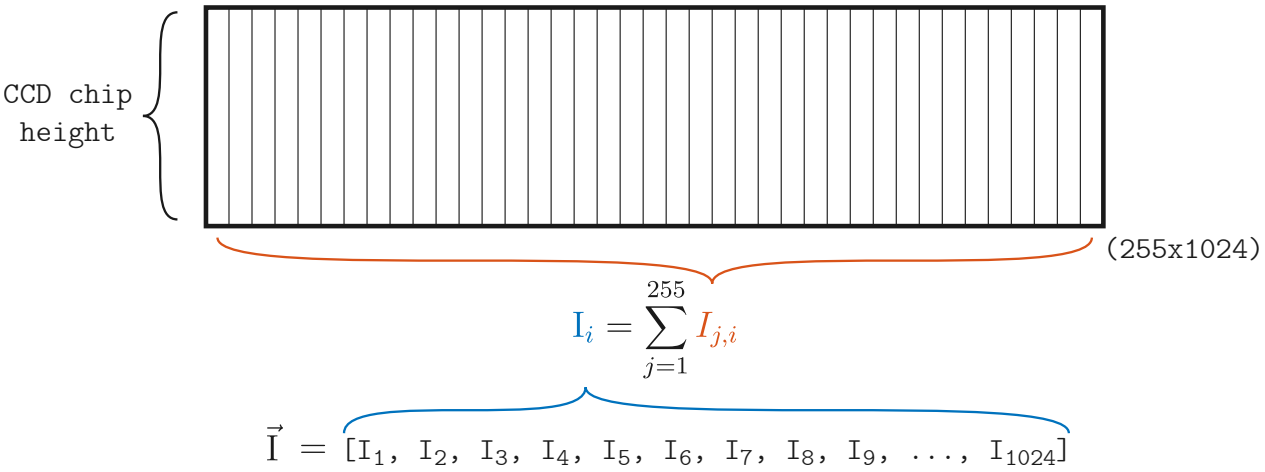

Figure 3.6 Visualization of Full Vertical Binning (FVB) read mode.

Acquisition mode refers to the different ways you can make acquisitions with the camera. Although it requires no additional parameters, **single scan** acquisitions are suboptimal for acquisition series of multiple spectra. In this mode, the camera would return acquired data to the computer after each scans, which takes around 150 ms. For example, an acquisition of 20 spectra with a 50 ms exposure time per spectra used to take $20 \times (150 + 50) = 4$ seconds with a total of 1 second of actual sensor exposure and 3 second of data transfer. Instead, cameras are now used in **kinetic series** acquisition mode. In this mode, the camera takes a single scan acquisition series and transfers the data only once the series has been completed. The same acquisition of 20 spectra and 50 ms exposure time now takes $20 \times (50) + 150 = 1.15$ seconds. As illustrated in Figure 3.7, the time required for short acquisitions has been significantly reduced. It is important to note that there is a 50 ms time buffer between the camera exposure start and the laser pulse to insure that the laser is *open* at the start of the acquisition series. For the same reason, the laser stays *open* 50 ms after the acquisition finishes.

Trigger mode specifies how camera acquisitions are triggered. When set to **internal trigger**, acquisitions are launched via a software command. Although slower ($\leq$ 5 ms) than **external trigger**, **internal trigger** does not require electrical connections between laser controller and the camera.

Shutter mode specifies how the camera shutter behaves. When set to "**open during FVB series**", the shutter opens as soon as the camera **read mode** is set to **FVB**. This is important when using the camera for **kinetic series** as it speeds up the acquisition. If a different **shutter mode** were used, the shutter would close and open between each spectra

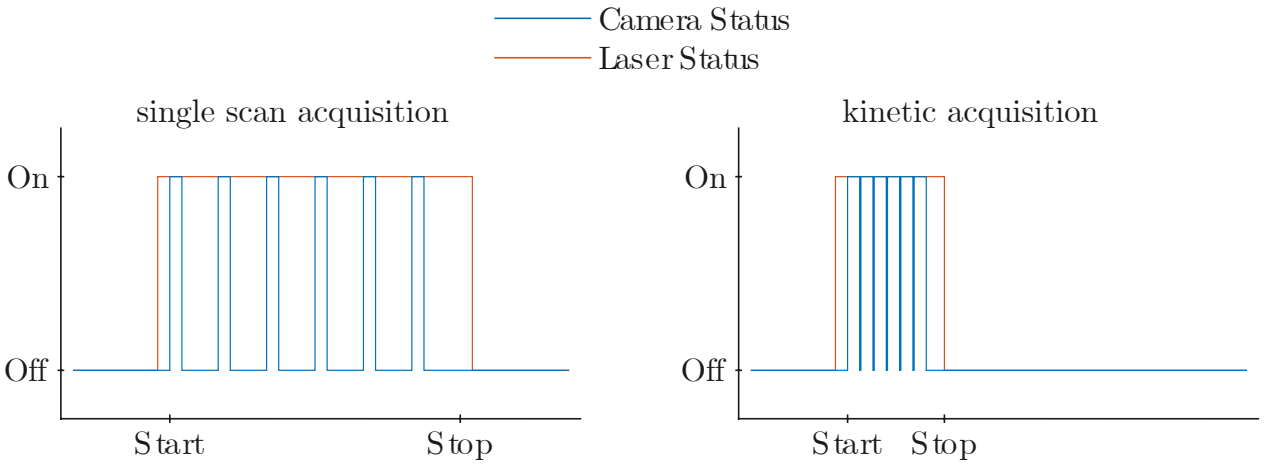

Figure 3.7 Comparison between **single scan** and **kinetic series** acquisition of six spectra, each with 50 *ms* of exposure time. This illustration mimics results obtainable with an oscilloscope connected to the *Andor camera's fire pin* and a *Thorlab PDA015A/M* photodetector.

during an acquisition which would take ~ 3 *ms* per spectrum.

It is possible to reduce the thermal noise during acquisition by lowering the camera sensor temperature. However, thermal noise reduction becomes negligible for **cooling temperature** $T \leq -60°\text{C}$. Since the camera cannot be cooled to temperature lower than $\leq -80°\text{C}$, it has been decided that a **cooling temperature** of $\leq -70°\text{C}$ should be used to reduce the risk of premature ageing of the camera.

3.1.3 TimByte Raman acquisition software

Finally, as a last step to modernize the Raman system, the acquisition software has been entirely reprogrammed from the ground up. The new acquisition software was programmed with *Matlab* and named *TimByte*. Writing the acquisition software with *Matlab* offered many advantages in comparison to *LabView*. In opposition to being *visual based*, *Matlab* is a *text based* programming language. This makes code development slower, but improves maintainability and upgradability. The high level object oriented syntax of *Matlab* allows for modular and flexible programming. Additionally, a Raman processing toolbox has been implemented in *Matlab* (Chapter 4) and seamlessly integrated with the acquisition software for real time display of processed spectra (Figure 3.8). In the future, real time classification results will be displayed to the user via the implementation of a classification tool box.

The resulting acquisition software has a 3-layer hierarchical structure. The top layer represents the Graphical User Interface (GUI) with which the user interacts to enter the different

acquisition parameters. The mid layer consists of a library of subGUI that interfaces with the bottom layer. The bottom layer is a library built to directly control the different devices either via their drivers or serial commands via USB. This hierarchy offers a robust platform for further development. New devices can easily be integrated to extend the use of *TimByte* to other techniques such as fluorescence or diffuse reflectance spectroscopy.

In addition, an *automatic exposure control* (AEC) algorithm has been implemented as an optional feature within the software. If enabled, the user enters three parameters: the *starting exposure* (exposure time [ms]), the *maximum exposure* (exposure time [ms]) and the *dynamic range target* ([0 to 100 %] corresponds to the sensor's 0 to $2^{16} - 1 = 65535$ intensity count). Then, the AEC algorithm will automatically set the exposure time within the minimum and maximum exposure limits that maximizes the dynamic range of the sensor according to the target. To do so, the software first makes a quick acquisition using the *starting exposure*, determines how much of the dynamic range is being used, linearly scales the exposure time by the factor necessary to reach the *target* without exceeding the *maximum exposure* and then proceeds with the complete acquisition.

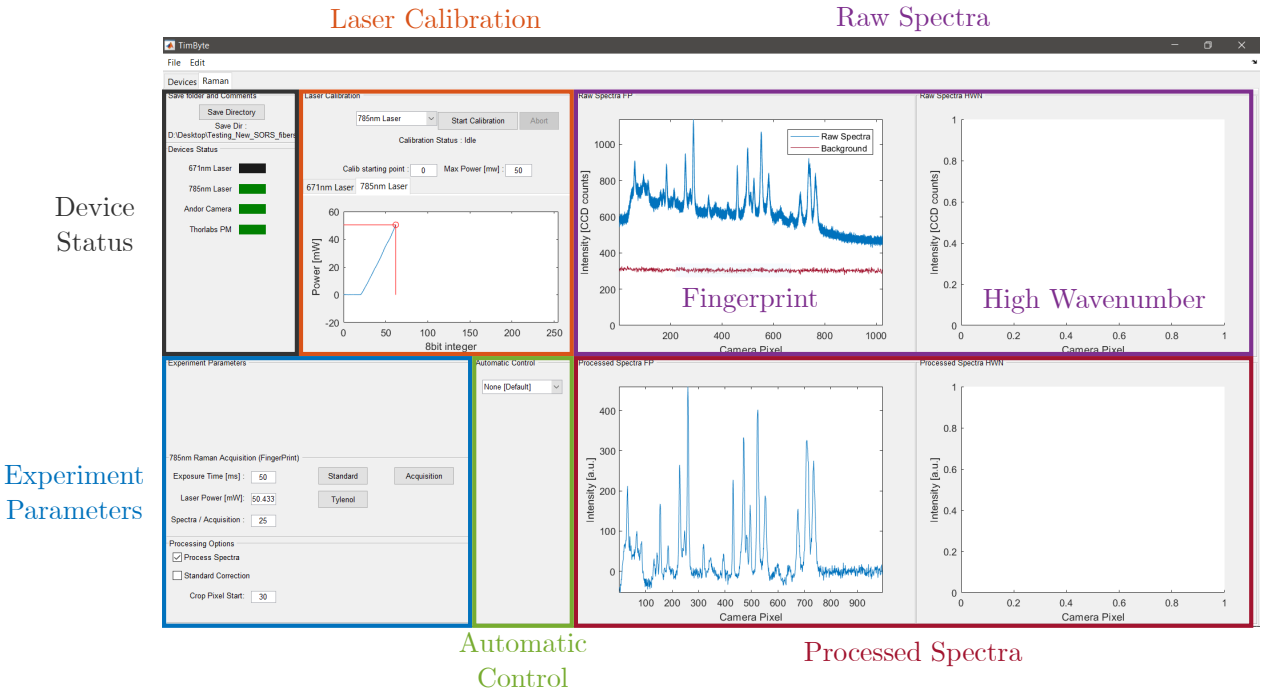

Figure 3.8 Screen shot of *Timbyte*'s acquisition window during a Raman measurement on Tylenol with the SORS bench presented in Chapter 5.

3.2 Results and validation

3.2.1 Laser calibration procedure

As mentioned earlier, a laser calibration procedure must be run at the beginning of every experiment. The goal of the calibration is to ensure that the laser power entered by the user is the actual power delivered to the sample through the instrument. To run a calibration, the user connects a *Thorlabs* power meter to the computer. Once the calibration starts, the software turns the laser on and progressively increases the power, recording at each step the actual power output of the instrument. Results are plotted and saved as calibration curves (Figure 3.9) that establish the relation between laser control input and instrument power output. Laser calibration takes around 1-2 minutes for *IPS* lasers and around 5 minutes for the *Laser Quantum* laser.

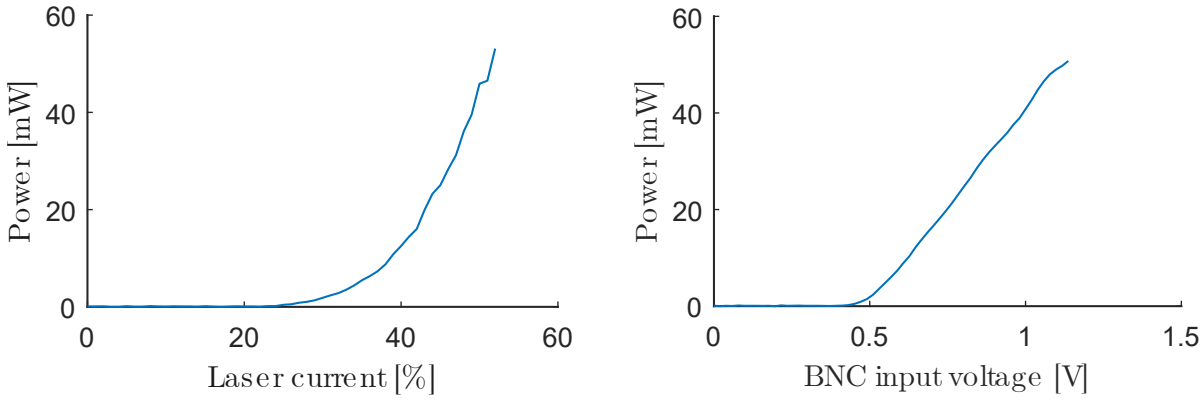

(a) 671 nm Laser

(b) 785 nm laser

Figure 3.9 Example of recorded laser calibration curves measured when using a handheld optical probe.

3.2.2 Linear response of the Raman system

Improvements made on the LRO Raman system allow to test that the Raman signal intensity increases linearly with exposure time and laser power. To do so, two series of Raman spectra have been acquired on Tylenol with a handheld probe. During the first acquisition series, the exposure time was fixed at $t_{exp} = 30$ ms and the output power was progressively increased from $P = 5$ mW to $P = 50$ mW. For the second series, the output power was fixed at $P = 30$ mW and the exposure time was increased from $t_{exp} = 5$ ms to $t_{exp} = 50$ ms. 100 spectra were taken per acquisition. Then, the 10 most prominent Tylenol peaks (Figure

3.10) are identified for each acquisition. The relationship between Raman signal intensity and acquisition parameters for each peak is displayed in Figure 3.11.

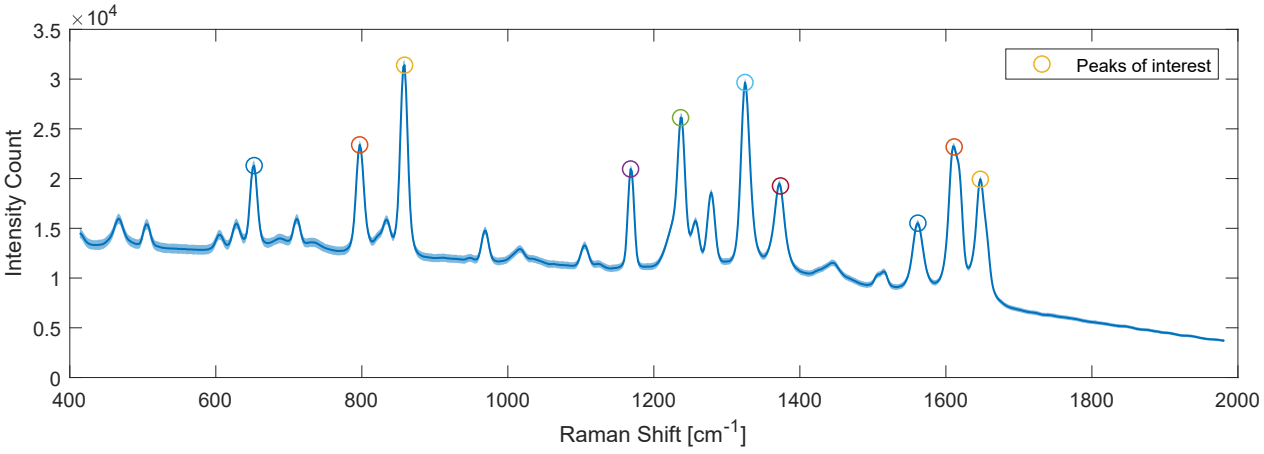

Figure 3.10 Tylenol Raman spectra acquired with a handheld probe [t_{exp} = 50 ms, P = 30 mW]. The *peaks of interest* are color coded for easier identification for Figure 3.11.

The averaged R^2 coefficient of a linear fit applied on the data with fixed laser power and fixed exposure is respectively $R^2 = 0.9997$ and $R^2 = 0.997$. Moreover, the average standard deviation of the intensity count over all 10 peaks for low exposure is smaller when using an exposure time of 5 ms and a laser power of 30 mW ($Std_{avg}(T = 5ms, P = 30mW) = 33$) than when using an exposure time of 30 ms and a laser power of $\sim$ 5 mW ($Std_{avg}(T = 30ms, P = 5mW) = 86$). This result suggests that even though the acquired signal can be linearly increased by either using longer exposure time or higher laser power, using small laser power is not advisable due to lower stability. Instead, the laser power should be set to the maximum value allowed by safety limits and the exposure time should be tuned by the user to maximize the camera's dynamic range.

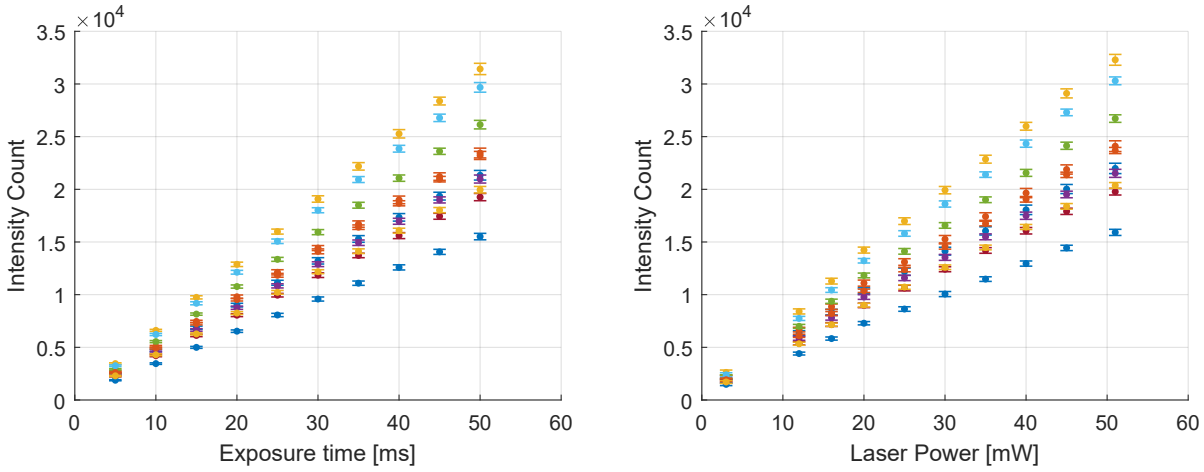

(a) Laser Power = 30 mW (b) Exposure time = 30 ms

Figure 3.11 Dependence of Raman signal intensity to exposure time and laser power for acquisition on Tylenol. The different colors can be used for peak identification in Figure 3.10.

3.2.3 Photobleaching of fluorescence

As a last experiment to validate the performance of the overhauled Raman system, the effect of *photobleaching* on tissue fluorescence has been investigated. *Photobleaching* refers to the weakening of fluorescence signal strength due to photochemical interaction between laser light and naturally fluorescent molecules present in biological samples. This phenomenon causes fluorescence background present on raw Raman spectra to fade off as samples are exposed to laser light. Accordingly, with properly optimized systems, raw spectra overall intensity should decrease progressively during an acquisition. To visualize the effects of photobleaching, Raman spectra have been acquired on pork fat tissue from a pork chop (Figure 3.12) with the Raman system post-overhaul and on calf's brains with the Raman system prior-overhaul (Figure 3.13). Spectra have been color coded to reflect their order during the acquisition. When comparing these results, it becomes clear that the laser and camera syncing issue that caused the acquired spectra intensity to artificially fluctuate has been resolved.

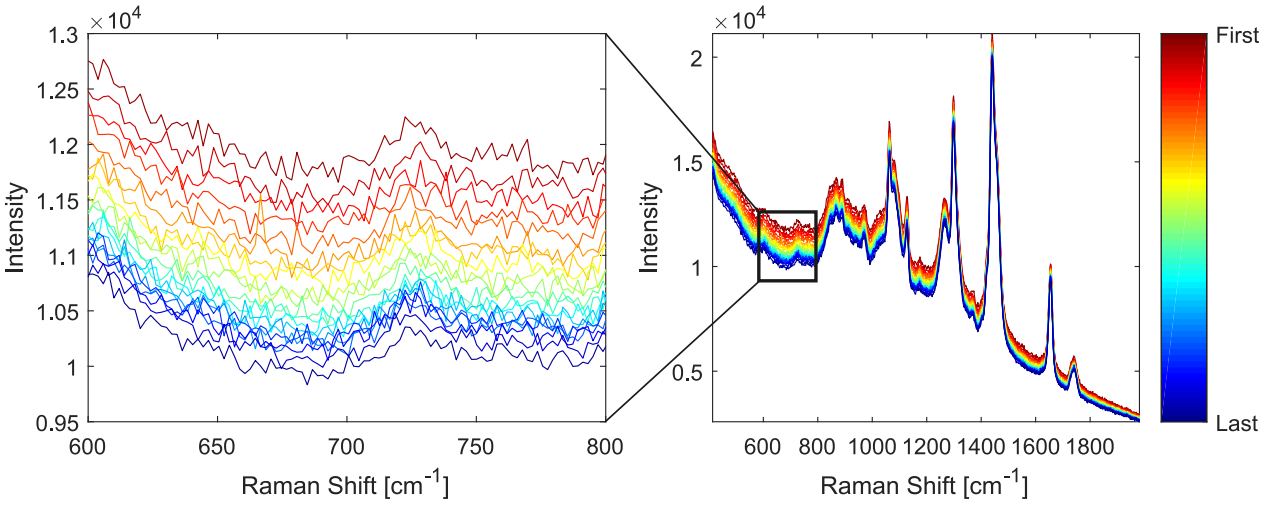

Figure 3.12 Raw Raman signal acquired on fatty tissue from a pork chop post overhaul of system.

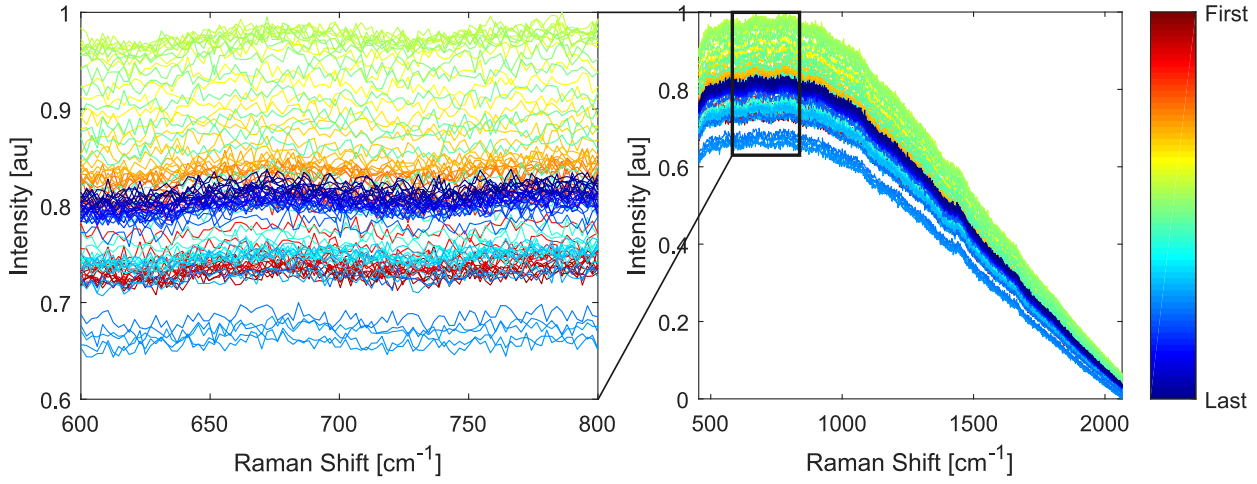

Figure 3.13 Raw Raman signal acquired on calf's brains prior to overhaul of system.

3.2.4 Summary of improvements

The work presented in this chapter significantly improved the quality of acquired spectra, ease of use of the system and general repeatability of experiments. Many technical problems with the system have been addressed and a few new useful features have been implemented. Table 3.2 presents a comparison between the specifications of the Raman system prior to and post overhaul.

Table 3.2 Specification of LRO Raman acquisition systems prior to and post overhaul. All specifications are given for an acquisition of 20 spectra, 50 ms exposure time (per spectrum) and 50 mW excitation power.

	prior to overhaul	post overhaul
Acquisition time	~ 4 sec	~ 1 sec
Excitation power	50 ± 30 mW	50 ± 2 mW
Actual power delivered to sample	Unknown	Known (within ± 2 mW)
Automatic control option	None	Automatic exposure control (AEC) Automatic power control (APC)
Real-time display of processed spectra	No	Yes
Metadata saved with acquisition	Laser output power (unreliable) Exposure time (unreliable due to desync) Comments	Date/time of acquisition (accurate to 100 ms) Laser calibration curve Sample excitation power Exposure time Camera temperature Automatic Control parameters (if used)

CHAPTER 4 RAMAN PROCESSING AND CLASSIFICATION TOOLBOX

This chapter covers the development and standardization of the LRO's Raman signal processing and classification toolboxes. To simplify its use and integration with *Timbyte* (Chapter 3), the toolboxes presented in this chapter have been written with *Matlab*. Every algorithm part of the toolboxes has either been implemented from scratch or based on the existing powerful *Maltab Statistics and Machine Learning Toolbox*.

4.1 Context and goal

Raw Raman spectra need to be processed before being analyzed or classified by a machine learning algorithm. Typical processing steps include the removal of cosmic rays (Section 4.2.2), a correction to account for the system response (Section 4.2.3) and the removal of the autofluorescence signal (Section 4.2.4). It has been well established that these three steps should always be performed as part of the Raman signal processing. However, different publications report different processing workflow. Often processing steps are used in different order or based on different algorithms. This results in an unfortunate issue; only spectra that went through the same processing procedure can be used as part of the same database for machine learning applications. In order to solve this problem, a unified and standardized Raman processing and classification toolboxes has been created. The end goal of these toolboxes was to offer a unified and standardized workflow for Raman spectra processing and classification. Accordingly, the following objectives have been formulated:

- Unify and standardize the LRO Raman signal processing workflow;
- Implement an automatic cosmic ray removal algorithm;
- Implement an automatic fluorescence removal algorithm;
- Create a unified classifier training workflow;
- Rewrite the existing classification toolbox to export trained classification models and feature reduction matrix for generalization testing.

4.2 Raman signal processing

The first half of this chapter presents the development and the current version of the LRO Raman signal processing toolbox. As explained earlier one of the main challenges to the

construction of large scale Raman spectra databases is the incompatibility of spectra that have been processed under different workflows. The principal cause of this problem is the lack of a well programmed, efficient and documented processing toolbox that is modular enough to easily be used with different acquisition systems. As a solution, two Raman signal processing workflows have been implemented and tested. The first one (Figure 4.1a) has been determined to be optimal for the processing of spectra acquired from samples presenting low levels of photobleaching whereas the second one (Figure 4.1b) should be used for spectra acquired from samples presenting high levels of photobleaching. More details are given in Section 4.2.2.

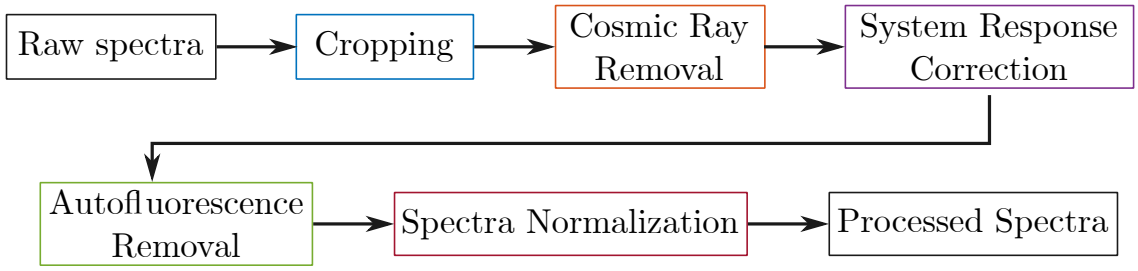

(a) For acquisitions with low photobleaching.

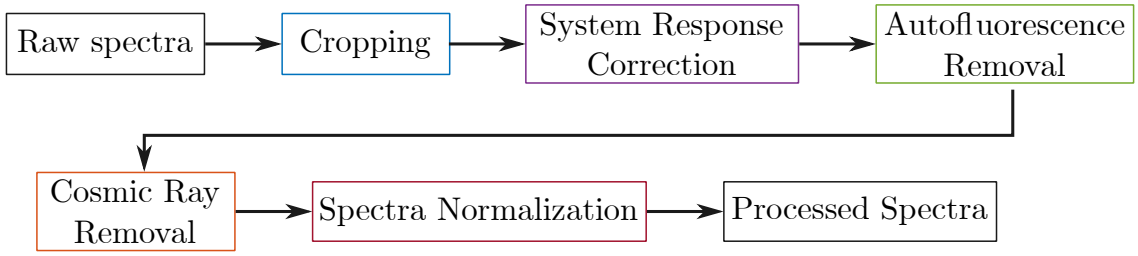

(b) For acquisitions with high photobleaching.

Figure 4.1 Raman signal processing workflow.

4.2.1 Spectrum Cropping

The first step in the processing of Raman spectra; *Spectrum cropping*, refers to the removal of the leftmost region of the acquired spectra. Since the spectrometer is never perfectly aligned with the first row of pixels of the camera, there is always a small region at the beginning of the spectrum that is unexposed and needs to be removed (Figure 4.2).

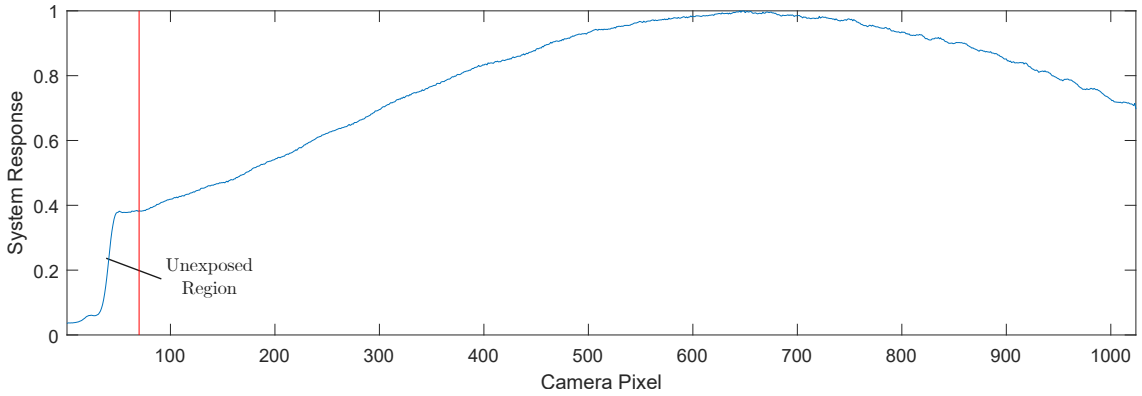

Figure 4.2 Unexposed region of the camera illustrated by the normalized system response spectrum acquired on the NIST Raman standard.

4.2.2 Cosmic ray removal

Cosmic rays are a type of high-energy radiations that generally originate outside our solar system [36]. In the context of spectroscopy, cosmic rays refer to occasional high energy photons that will hit the camera sensor and saturate a pixel or a group of pixels during an acquisition (Figure 4.3a). Although this does not often happen, the longer an acquisition is, the more likely cosmic rays are to be recorded. This becomes especially problematic for Raman spectroscopy as cosmic rays can be mistaken for Raman peaks. Fortunately, the following procedure proves to be very effective to identify and remove cosmic rays for acquisitions of multiple spectra from samples exhibiting low levels of photobleaching.

1. Compute the Raman intensity standard deviation (STD) for the acquisition (Figure 4.3b).

2. Identify wavelengths in the spectra where cosmic rays might have been recorded by using a peak finding algorithm.

3. Identify which spectrum has the highest intensity value for each wavelengths identified in 2 (Figure 4.3c).

4. Either:

    - Discard the spectra that have been flagged with a cosmic ray.
    - Replace the intensity values from the region where the cosmic ray has been detected with a linear interpolation (Figure 4.3d).

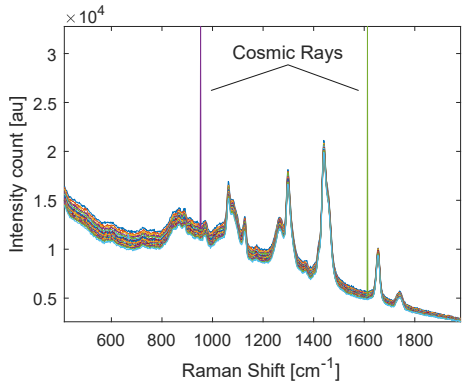

(a) Raw spectra with 2 cosmic rays

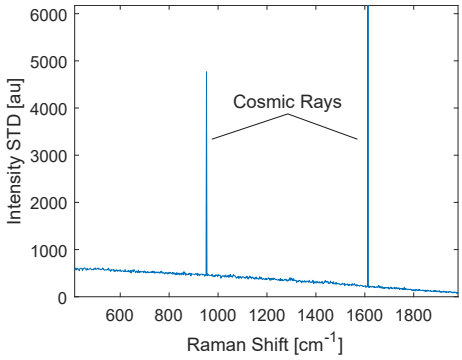

(b) Spectra intensity STD

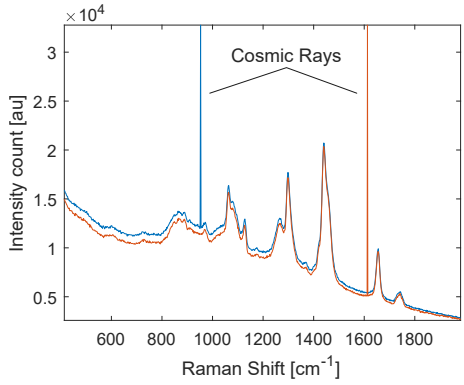

(c) Identified spectra with cosmic rays

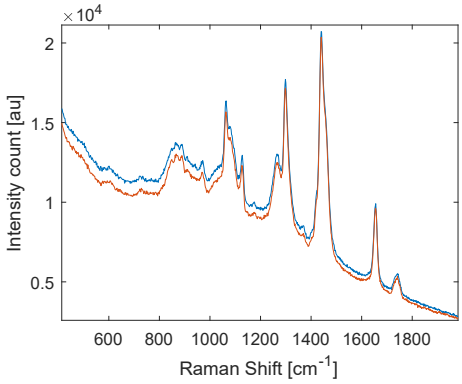

(d) Identified spectra after cosmic rays are removed

Figure 4.3 Cosmic ray removal algorithm demonstrated on pork fatty tissue acquired from a pork chop with a handheld Raman probe.

When it comes to samples presenting high levels of photobleaching, it is advisable to proceed with the removal of cosmic rays after the autofluorescence signal has been removed. Otherwise, the higher overall intensity STD induced by the photobleaching can easily introduce erroneous identifications for step 2. and 3.

4.2.3 System response correction

Different Raman acquisition systems have different responses. Either caused by the uneven wavelength-dependent transmission of the optical instrument or the detector quantum efficiency, significant variations can be observed on Raman spectra acquired with different systems on a given sample. These variations can become particularly large when different laser wavelengths are used. This issue is typically solved by applying a relative intensity correction to the measured spectra [37]. To obtain the system response, it is possible to measure

the Raman spectrum of a Standard Reference Material (SRM) manufactured by the National Institute of Standards and Technology (NIST). The NIST SRM 2241 relative intensity correction standard for instance, produces a uniform Raman signal when excited with a 785 nm laser. This means that the Raman acquisition system response can be obtained simply by measuring the Raman signal from the NIST SRM 2241 (Figure 4.4a). Acquired Raman spectra are then divided by the system response to apply the correction (Figure 4.4b).

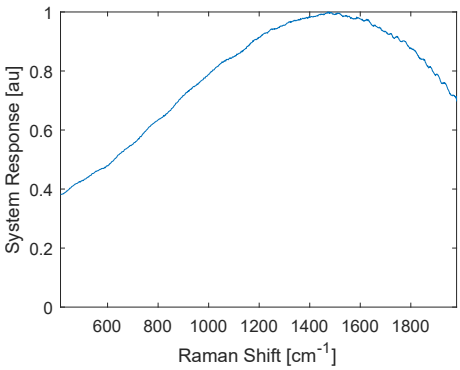

(a) Typical system response

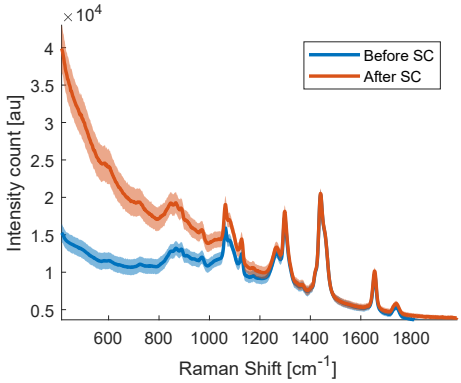

(b) Spectra before and after system response correction (SC)

Figure 4.4 System response correction algorithm demonstrated on pork fatty tissue acquired from a pork chop with a handheld Raman probe.

4.2.4 Autofluorescence removal

Autofluorescence removal is possibly the most important step for Raman signal processing. Autofluorescence signal can often take more than half of the dynamic range of the camera when acquiring Raman signal from biological samples (Figure 4.5a). Moreover, removing autofluorescence without affecting the remaining Raman signal proves to be very difficult. Recently, an iterative method based on the Savitzky-Golay filter has shown remarkable results for removing autofluorescence and for denoising Raman spectra [38, 39]. However, the longer algorithm computing time (~ 0.5 sec/spectrum) of this method proved problematic for real time display of processed spectra ($\sim 1.5-2$ sec for ~ 20 spectra) with TimByte (Chapter 3). Instead, an older, simpler and faster algorithm was implemented and modified; the ModPoly algorithm [40]. By combining a multi-polynomial fitting with a peak-removal procedure, the ModPoly algorithm could serve as an autofluorescence removal algorithm that can be used for real-time application. The implemented version corresponds to the original ModPoly algorithm [40] with a modified stop condition. In addition to the original stop condition, the implemented version also counts the number of iterations and will stop if the *timeout*

parameter is reached. This modification was included specifically for real-time use with TimByte. In addition, the desired polynomial fit order [default = 6] can be specified when using the algorithm. The autofluorescence removal algorithm is demonstrated in Figure 4.5.

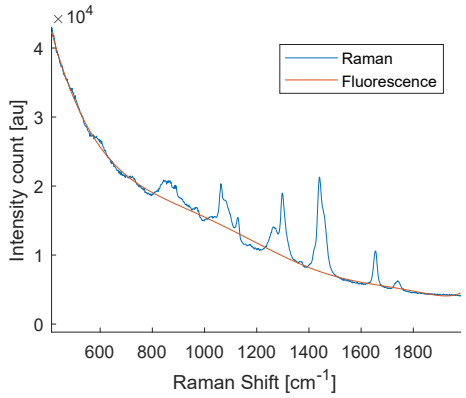

(a) Raman spectra and autofluorescence signal estimated by the ModPoly algorithm

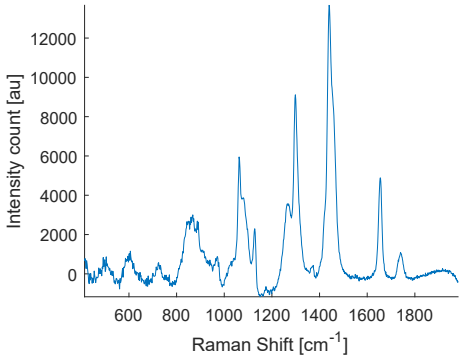

(b) Raman spectra after autofluorescence removal

Figure 4.5 Autofluorescence removal algorithm (AFR) demonstrated on pork fatty tissue acquired from a pork chop with a handheld Raman probe.

4.2.5 Spectra normalization

The last Raman signal processing step consists of an optional spectrum normalization. In opposition to the system response correction that scaled the Raman spectrum by a different factor for each wavelength, the spectrum normalization is a single scaling factor applied to the entire spectrum. This normalization factor serves the purpose of expressing processed spectra on a comparable scale when dealing with spectra acquired with different acquisition parameters. Prior to this work, the acquisition parameters recorded in the metadata of the acquisition was incomplete and unreliable. Thus, only mathematical based normalization could be used, such as Area Under Curve (AUC = 1) normalization (Figure 4.6a). Since mathematical based normalization doesn't take acquisition parameters into account, direct intensity comparison between spectra loses all meaning leading to worse classification performance (Section 4.3). Now that the LRO Raman acquisition system has been shown to have a linear response with laser power and exposure time (Chaper 3), normalizing spectra by their acquisition parameter is possible (Figure 4.6b). By dividing the spectrum intensity by the laser power and exposure time, it can be expressed on a scale for which all spectra acquired with the same system are comparable. This also means that when dealing with spectra that were all acquired with the same laser power and exposure time, no normalization is necessary.

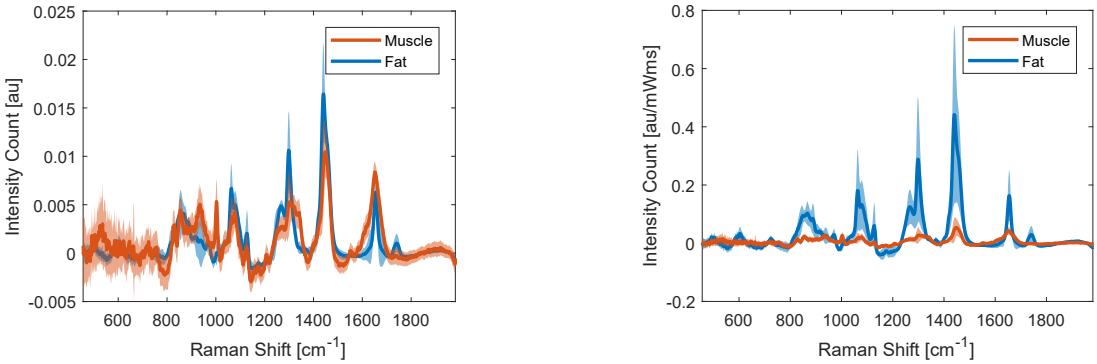

(a) AUC normalization

(b) Exposure normalization

Figure 4.6 Processed Raman spectra of pork muscle and fat tissue acquired from a porkchop with Area Under Curve normalization and exposure normalization.

4.3 Raman spectra classification

The second half of this chapter presents the development and upgrade of the LRO machine learning toolbox designed for Raman spectra classification. The existing classification toolbox used within the LRO prior to this work served as a solid foundation for the new version. Although the previous version of the toolbox had an intuitive and simple graphical user interface, the lack of many software features and development choices limited its use. Namely, the following features were missing from the toolbox

- Trained classification models couldn't be exported;
- No feature basis transformation matrix was computed or saved when using a feature reduction algorithm;
- The toolbox main GUI was implemented using Matlab's GUI Development Environment (GUIDE) - a graphical GUI development tool.

The first two issues made it impossible to test trained classification models on new data. The third issue limited the integration of better data and performance visualization tools. Because GUI developed with GUIDE are limited to a small number of graphical elements, and because the GUIDE environment consist of a graphical interface, the previous toolbox GUI was difficult to maintain, tedious to modify and incompatible between Matlab versions. Accordingly, the classification toolbox was remodeled and renamed *ZenClass*. The toolbox backbone was reprogrammed to implement the new classification workflow (Section 4.3.1) and the main GUI was rewritten as a class (object oriented notation) to improve its upgradability, portability, performance and stability.

4.3.1 Classification workflow

The classification workflow presented here has been developed for a very specific reason: investigate the generalization of trained Raman spectra classifiers. When it comes to classifiers and machine learning in general, a simple question always remain; how well can a trained model generalize to unseen data? Unfortunately, it is so far impossible to provide a general answer to this question. Thus, every trained model should be tested. In order to provide a tool to easily train and test classification models on Raman spectra, a new classification workflow has been implemented (Figure 4.7).

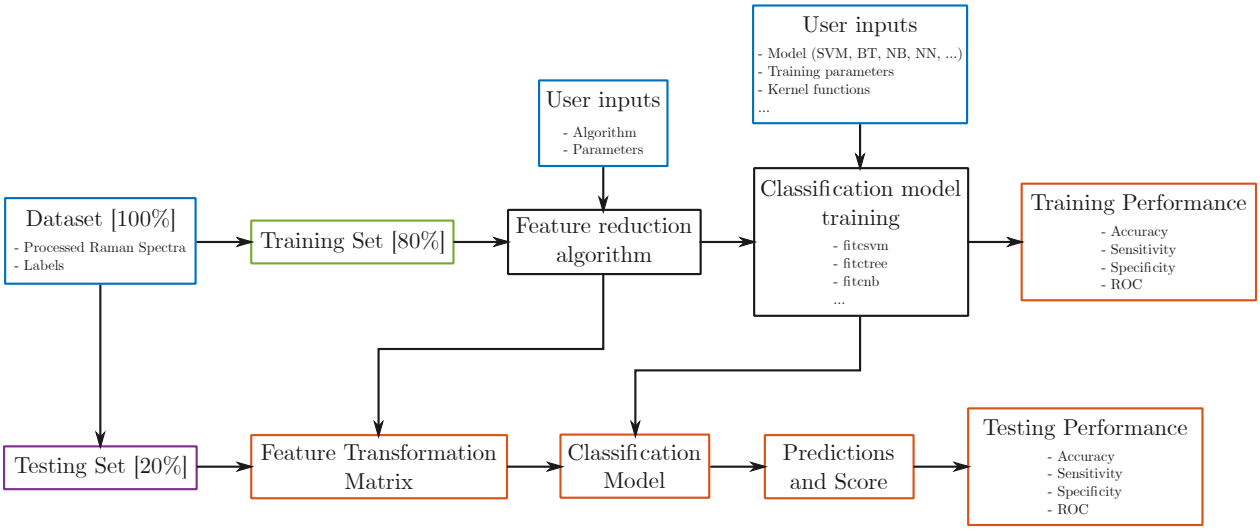

Figure 4.7 LRO classifier training workflow.

Starting with a *complete* dataset of processed raman spectra and their respective labels, a *training set* and a *testing set* are created. Typically, 80% of the original dataset will be used for training and 20% will be used for testing. At this point, a feature reduction algorithm (Section 4.3.2) is used on the *training set*. The outputs of the feature reduction are the *training set* expressed in a transformed vector space and the transformation matrix that transformed the original vector space to the transformed vector space. Then, a classification algorithm is trained on the *training set* (Section 4.3.3). The outputs of the classification model training are the trained classification model and the performance metrics computed on the training set. Common performance metrics are the accuracy [%], the sensitivity [%], the specificity [%] and the ROC curve. After the training phase comes the testing phase where the testing data is expressed in the transformed vector space with the feature transformation matrix. The classification model is used on the testing data and outputs class predictions and scores. These predictions are compared to true labels to obtain the performance metrics

computed on the *testing set*. By comparing the performance of the model on the *training set* and *testing set*, it is possible to diagnose training problems such as underfitting and overfitting, but most importantly it is possible to evaluate how well the model generalizes to unseen data.

4.3.2 Feature Reduction

Feature reduction refers to the use of both *feature engineering* and *dimensionality reduction* algorithms. The basic idea behind it is simple; is it possible to reduce the number of variables (features) considered by the classification model without affecting its performance? With Raman spectroscopy, it often happens that spectra acquired from different tissues have very similar signals within some spectral bands and very different signals for others (Figure 4.8). It may be possible to significantly reduce the number of acquired wavelengths without decreasing the classification performance. Reducing the size of the feature space also significantly reduces the risk of model overfitting

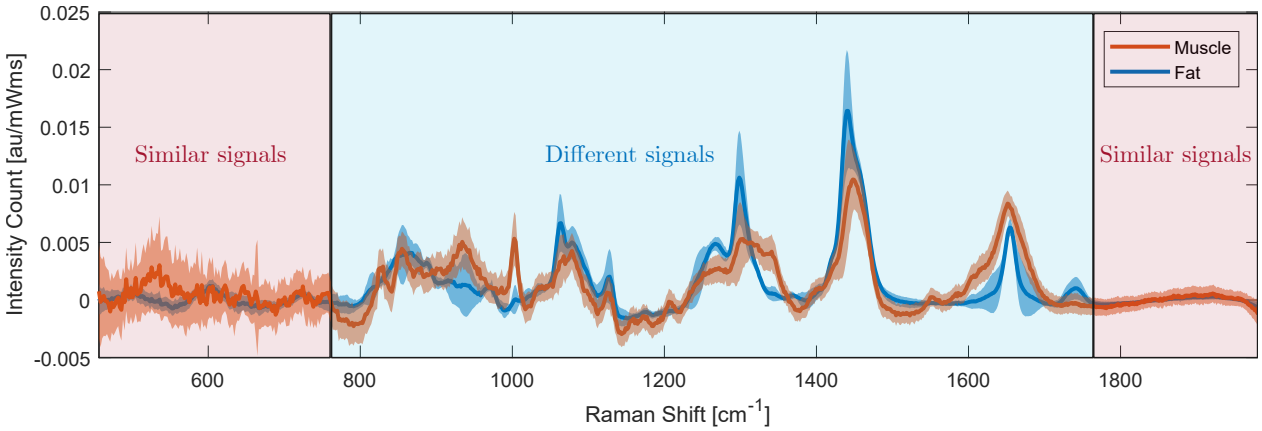

Figure 4.8 Illustration of differences and similarities between Raman spectra acquired from different tissues.

Since many different dimensionality reduction and feature extraction algorithms are already implemented as part of *Maltab Statistics and Machine Learning Toolbox* and because no original feature reduction algorithms as been developed in this work, detail about how these algorithm work will not be discussed with the exception of Matlab's ReliefF algorithm used in section 4.3.3. To rank features (spectrum wavelengths) in order of significance for the classification, the ReliefF algorithm iteratively computes their weights. ReliefF first gives each feature a weight of 0. Then, each weight is updated by iteratively selecting a random observation (spectra) and finding the k-nearest observation of each class. The algorithm then

penalizes (lowers the weight of) the features that give different predictions to neighbours of the same class, and rewards (increases the weight of) features that give different predictions to neighbours of different classes. Once the weights have been computed, it is possible to rank the features in order of relevance for classification (order of decreasing weights). It is also important to mention that every feature transformation algorithm can be modelled as a basis transformation matrix (Equation 4.1). For example, when using ReliefF, the transformation matrix is a matrix of ones and zeros that reorders the features in order of decreasing weights.

$$\underbrace{\begin{bmatrix} -Spectrum_1- \\ -Spectrum_2- \\ -Spectrum_3- \\ \dots \\ -Spectrum_n- \end{bmatrix}_{n\times k}}_{\text{Transformed Feature Space}} = \underbrace{\begin{bmatrix} -Spectrum_1- \\ -Spectrum_2- \\ -Spectrum_3- \\ \dots \\ -Spectrum_n- \end{bmatrix}_{n\times m}}_{\text{Original Feature Space}} \cdot \underbrace{M_{m\times k}}_{\text{Basis Transformation Matrix}} \tag{4.1}$$

Once $M_{m\times k}$ has been computed, it can be used to transfer any data from the original feature space to the transformed feature space.

4.3.3 Classification model training

Similarly to feature reduction algorithms, classification model training functions are already implemented in *Maltab Statistics and Machine Learning Toolbox* and will not be discussed. Although algorithm training can be done automatically, the user must still choose a classification model and set the training hyperparameters. Unfortunately, choosing classification models and training hyperparameter remains a tedious process of validation and optimization for which the goal is to obtain the best performing classifier. In order to compare trained models and identify the best model, a performance metric needs to be defined. As explained in Chapter 2, ROC curves can be used to illustrate the diagnostic ability of a binary classifier and the area under the ROC curve can be used as a good performance metric.

As an example, SVM classifiers have been trained on Raman spectra acquired with a handheld probe on pork muscle and fatty tissue from a porkchop. Raw spectra were processed with the workflow presented in Figure 4.1b with the exception that each spectrum was normalized relative to their maximum ($max(I(RS)) = 1$). Otherwise Raman spectra were linearly separable and every trained SVM classifier would give a perfect score (Figure 4.6b). Although this is great in practice, it makes for a poor classifier benchmark. By using *Matlab's Relieff* feature reduction algorithm, the features were ranked from the most significant to the least significant relative to the classification performance. The SVM classifiers were trained using:

a number of features $N = 1, 5, 10, 50$ and 935 (all); a linear kernel; and were validated with k-fold cross validation ($k = 10$ folds here). The training process was repeated 10 times with a new randomized *training set* and *testing set* for each iteration. Presented in Figure 4.9, the results indicate that only 50 features are necessary to achieve a perfect score on both the *training set* and *testing set*. In addition, using more features does not increase performance and may increase the risk of overfitting for this particular dataset. Finally, since the area under the training and testing ROC curves are identical for SVM classifier trained with 5 features and more, the trained models generalize well to unseen data.

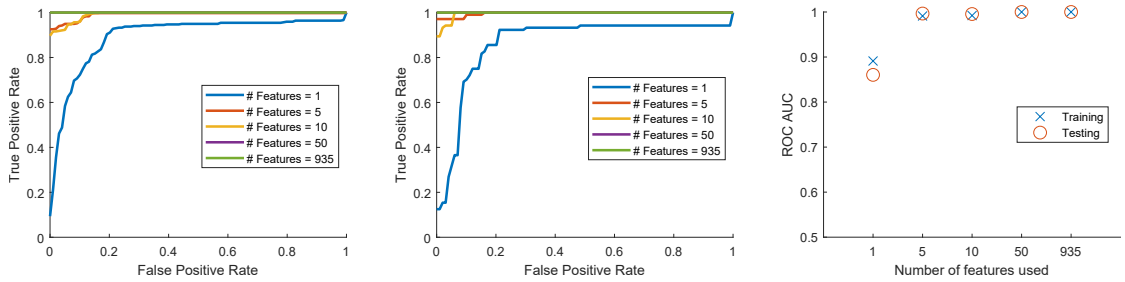

(a) Training Set ROC curve (b) Testing Set ROC curve (c) Area under ROC curve

Figure 4.9 SVM classifier training results on pork tissue classification.

4.3.4 ZenClass classifier training GUI

The final step in the rework of the LRO spectra classification toolbox was the integration of the toolbox backbone presented so far to toolbox main GUI. Although the integration is not yet complete, the main GUI has been rewritten and can be used to load and visualize training data, to select feature reduction and classification algorithms, to train classification models and to visualize performance (Figure 4.10). However, some software features still need to be integrated, such as

- A control panel to set model training parameters;
- A control panel to set feature reduction parameters;
- A control panel to create training and testing sets within the GUI;
- A display panel to plot the testing set ROC curve.

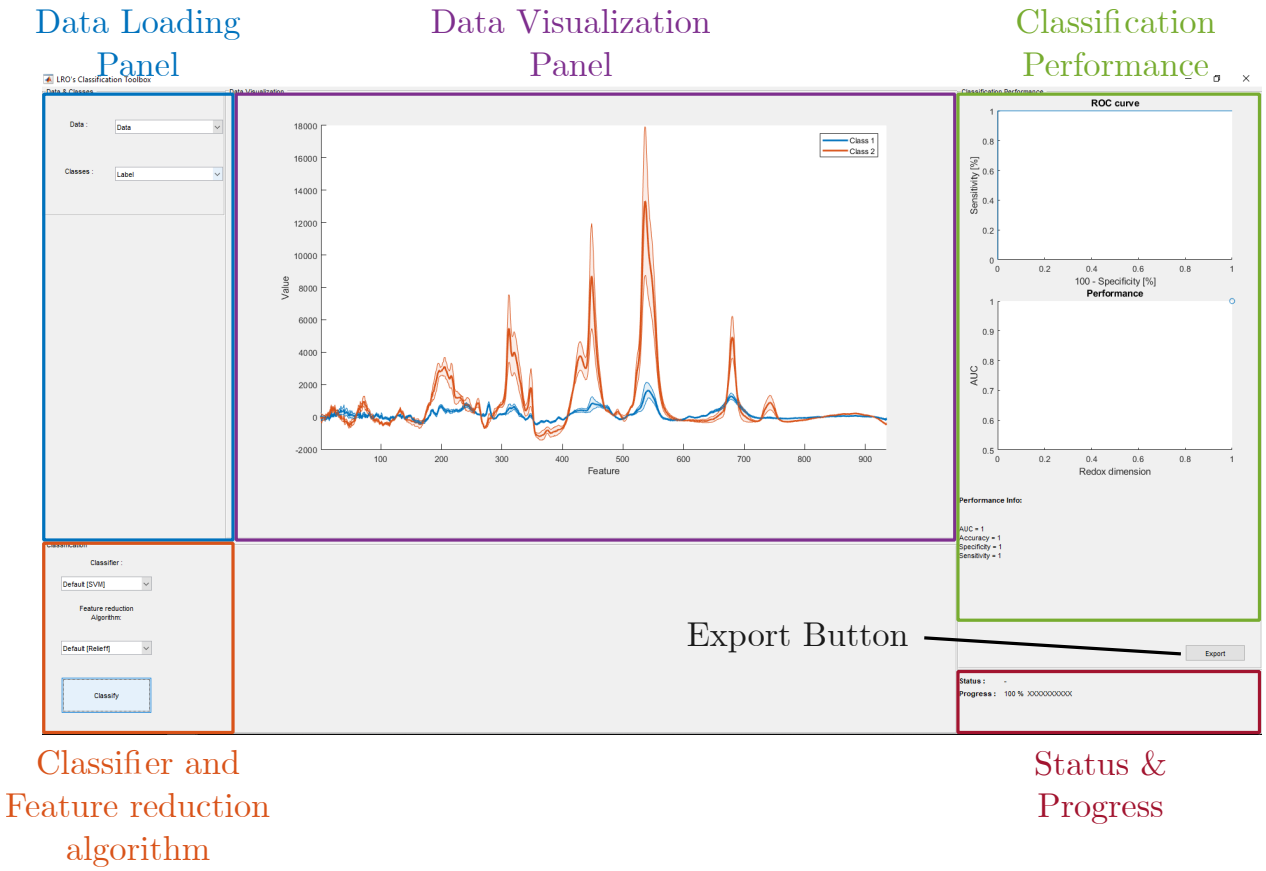

Figure 4.10 Screen shot of *ZenClass* classifier training main GUI.

CHAPTER 5 SORS CARACTERIZATION PLATFORM

This chapter covers the details of a SORS characterization platform built to investigate how the core diameter, numerical aperture and the spatial offset between an emission and collection fiber affect the Raman signal acquired on two-layer optical phantoms.

5.1 Context and scientific problematic

Conventional handheld Raman probes, such as the one used for this project, are reliable tools for characterization of biological tissue. They can provide highly specific and localized chemical information from probed samples while being minimally invasive and non destructive. However, the penetration depth of a conventional probe is limited to the first ~ 100 μm acquiring spectra from biological samples. Spatially Offset Raman Spectroscopy (SORS) probes can be used to increase the effective probing depth of Raman spectroscopy. As discussed in Chapter 2 it is possible to increase the penetration depth of the collected light in diffusely scattering samples by modifying the probe design and offsetting the excitation and collection fibers (Figure 5.1). Recently published work demonstrated the use of SORS probes to analyse the composition of bone tissue from canine limbs [13] and for breast tumor margin evaluation [11, 14, 17]. Unfortunately, no consensus has been reached regarding what spatial offsets should be used for biological applications. In fact, since the probing depth of SORS probes also depends on the optical properties (μ_a, μ_s and n) of samples and the ideal probing depth changes for each applications, there is no optimal spatial offset in general. This means that every time a SORS probe is designed for a clinical application, the choice of spatial offset and fiber numerical aperture (NA) is essentially an educated guess.

The SORS characterization platform presented in this chapter was built to address the following questions

- How does the fiber offset affects the Raman signal acquired from two-layer phantoms with different optical properties?
- How does the fiber numerical aperture (NA) affects the penetration depth of the SORS signal?

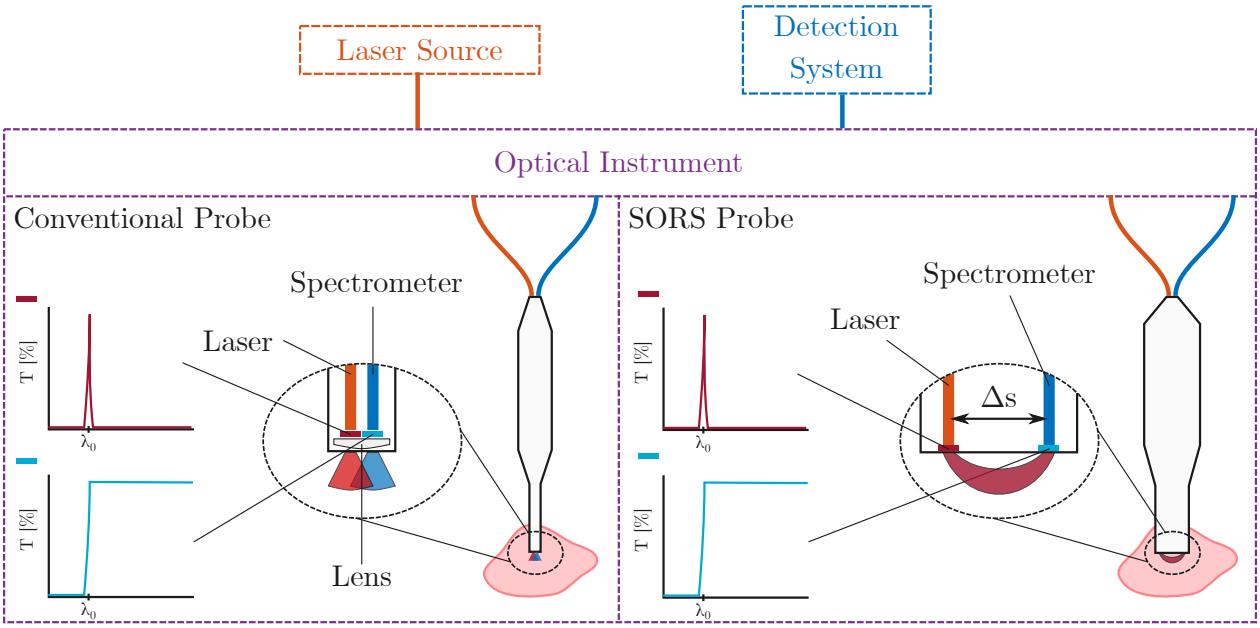

Figure 5.1 Comparison between typical components of a "conventional" Raman probe and a SORS probe.

5.2 Design and construction

In order to address the stated problematic, the SORS platform needed to

- be compatible with the LRO's Raman systems presented in Chapter 3;
- allow easy replacement of excitation and collection fibers (to test effects of fiber NA);
- have a maximum spatial offset range of at least 10 mm;
- have a minimum spatial offset increment smaller than 50 μm;
- have an absolute spatial offset on-axis accuracy smaller than $\pm$25 μm.

The developed SORS platform (Figure 5.2) is constituted of three basic elements detailed in this section; a translation stage, filter tubes and fiber holders.

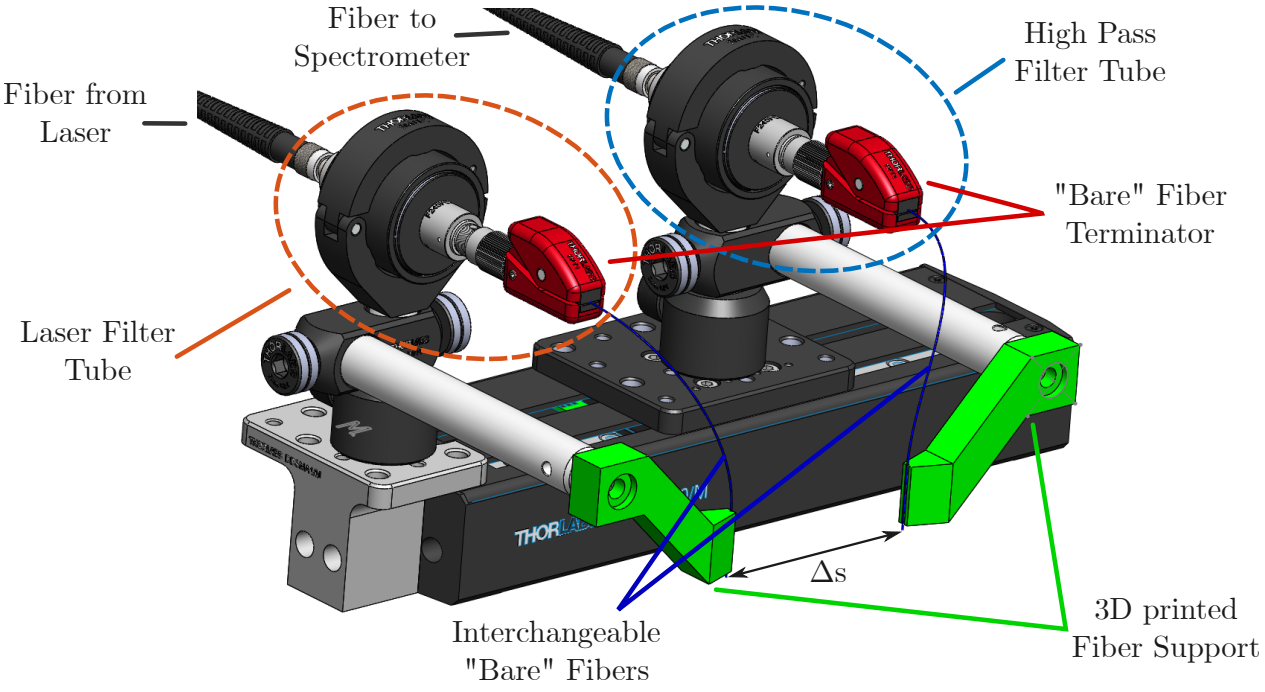

Figure 5.2 Hardware schematic of the final SORS testing platform.

5.2.1 Translation stage

The central component of the SORS platform is the translation stage. It defines most specifications related to the spatial offset. The best option considered was *Thorlab's DDSM100/M* linear translation stage as it's specifications (Table 5.1) far exceed the initial requirements. Moreover, since it comes fitted with mounting plates drilled and tapped with M6 holes, it is compatible with most optomechanical components.

Table 5.1 Specification of Thorlab's *DDSM100/M* linear translation stage (from *DDSM100/M*'s user guide).

Parameter	Value
Travel Range	100 mm
Velocity (Max)	500 mm/s
Acceleration (Max)	5000 mm/s
Min Incremental Movement	500 nm
Absolute On-Axis Accuracy	± 5.0 μm

5.2.2 Filter tubes

The second component of the SORS platform is the filter tube. As mentioned in Chapter 2, filters are critical to Raman optical instruments. The laser emission spectrum must be narrow to maximize the spectral resolution of acquired Raman spectra and the Rayleigh scattered light from the sample must be filtered out from the collected signal to maximize the camera's dynamic range. To achieve this, two filter tubes have been designed (Figure 5.3). For the laser filter tube, the light is delivered from the laser via a conventional SMA-SMA fiber patch cord. It is then collimated to a free space beam, passes through a laser clean-up filter and reinjected into the output *bare* fiber (Laser → filter tube → sample). The high pass filter tube is similar with the exception that a high pass filter is used and that light travels in the opposite direction (sample → filter tube → spectrometer).

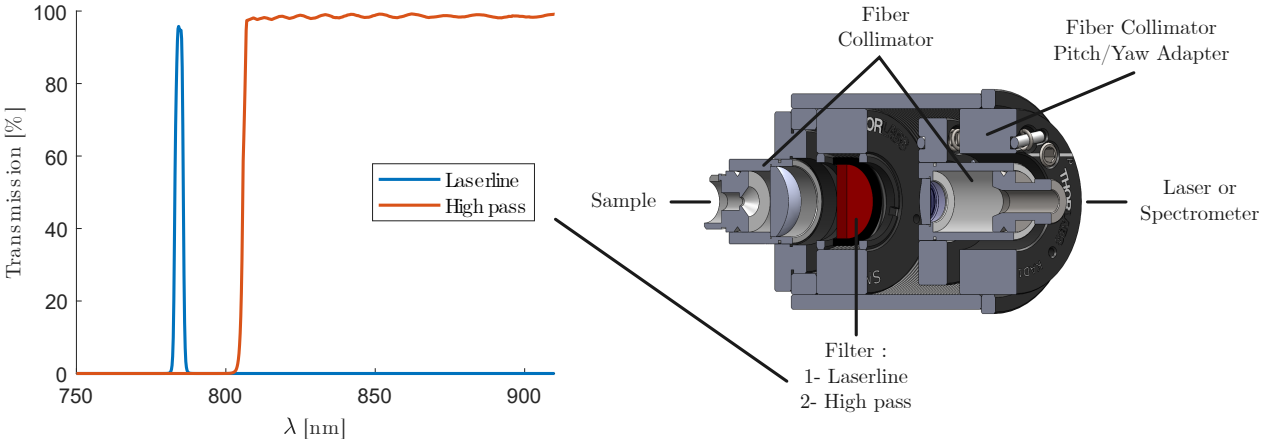

Figure 5.3 Schematic and response of the optical filter tubes used with the SORS platform.

5.2.3 Fiber holders

The last component of the SORS platform is the *bare* fiber holders. The holders were designed with the CAD software *Solidworks* and 3D printed in *polylactic acid* (PLA). In order to be able to bring the excitation and collection fiber adjacent to one another ($\Delta s = 0$), the fibers needed to be glued to the holders. The holder was designed with a central groove along its length that secures the fiber and creates more surface area for the glue to hold on to, thus making the bond stronger. The complete procedure to fasten a fiber to the holder is as follows

1. Cut a length of $\sim$ 20 cm of bare fiber.

2. Remove $\sim$ 3 cm of coating on each end of the fiber with wire strippers.
3. Cleave each end of the fiber to make a clean termination.
4. Clean both stripped ends of the fiber with isopropyl alcohol.
5. Apply a drop of cyanoacrylate glue along the fiber holder groove.
6. Carefully press the fiber inside the groove and hold until the glue dries.
7. Apply another drop of glue on top of the fiber.

When gluing the fiber to the holder, the fiber should be held so that there is a $\sim$ 1 mm clearance between the fiber tip and the bottom of the holder (Figure 5.4). The clearance insures that the fibers can be brought arbitrarily close to the sample without the holder touching it. Additionally, once the fibers have been glued, the assembly must be manipulated with extreme caution. The fibers are extremely fragile at each end of the holder and will snap easily if pulled.

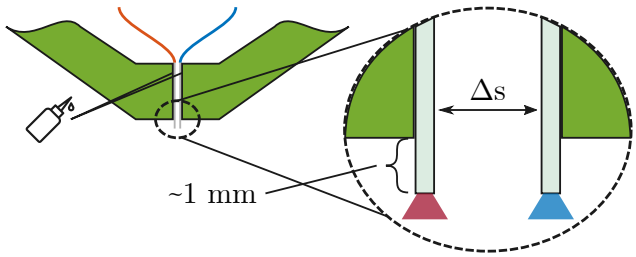

Figure 5.4 Illustration of the SORS platform fiber holders.

5.3 Validation on optical phantoms

The SORS platform was designed to investigate the use of a SORS probe in the context of tissue interrogation. For instance, a SORS probe could be used to detect the presence of cancerous tissue through a thin layer ($\sim$ 500 μm) of healthy tissue (Figure 5.5). This modality can be tested by using the SORS platform with a two-layer optical phantom, where the top and bottom layers of the phantom represent healthy and cancerous tissue respectively. Many different techniques exist to achieve the creation of a tissue mimicking phantom. Depending on the desired application, optical phantoms can either be solid or liquid. However, only solid phantoms can achieve a two-layer separation that is well defined and stable over time. Solid optical phantoms are typically made from a base material chosen for its mechanical

properties to which are added scattering and absorbing agents. In SORS applications, it is also necessary for the top and bottom layer to have different Raman signatures.

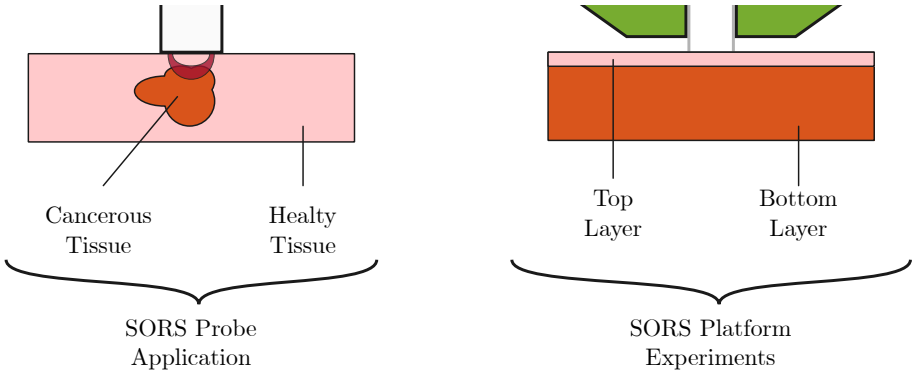

Figure 5.5 Illustration of a SORS probe used in the detection of cancerous tissue hidden below healthy tissue and of a SORS platform experiment to test the same modality.

5.3.1 Nylon-PDMS phantom fabrication

Nylon and polydimethylsiloxane (PDMS) were the chosen materials to build the SORS two-layer phantoms. Both materials have distinct Raman signatures (Figure 5.6) and are readily available. Additionally, the use of PDMS for the creation of a solid optical phantom has already been well documented [41–43].

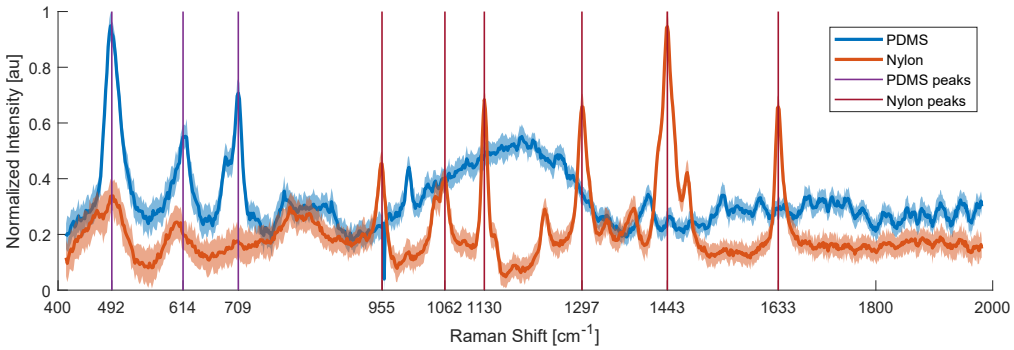

Figure 5.6 Pure Raman spectra of Nylon and PDMS acquired with the SORS platform fitted with 400 μm 0.5 NA fibers with no offset.

The two-layer phantoms were constructed by using nylon as the bottom layer and PDMS as the top layer. For the bottom layer, a nylon rod (diameter = 1 in., length = 12 in.) was cut into several nylon disks (diameter = 1 in., thickness $\simeq$ 1 cm). For the top layer, a

PDMS elastomer base (*Sylgard® 184 Silicone Elastomer Base*) is mixed with a PDMS curing agent (*Sylgard® 184 Silicone Elastomer Curing Agent*) in a 10:1 mass-to-mass ratio. Prior to mixing, TiO_2 powder is added to the curing agent to increase the scattering coefficient of the PDMS. The PDMS/TiO_2 mix is then placed in a vacuum for an hour or until all the bubbles have been removed. The PDMS is poured and spin coated on the nylon disks. The spin coating procedure insures a uniform thickness of PDMS (Figure 5.7). Finally the nylon/PDMS phantom is placed in an oven at 80° C until the PDMS has fully cured.

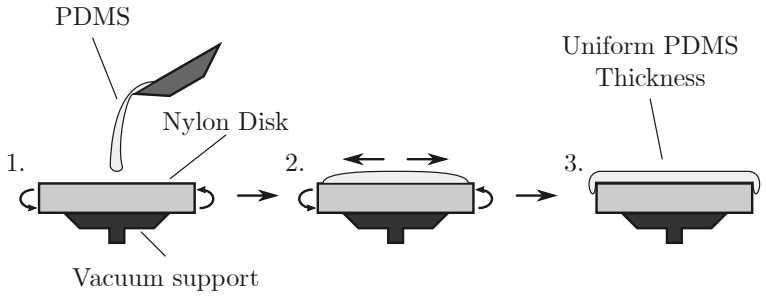

Figure 5.7 Illustration of the spin coating procedure.

Among all phantoms made this way, four were kept for SORS experiment, each with a different TiO_2 concentration. Properties of the used nylon-PDMS phantoms were measured and are presented in Table 5.2.

Table 5.2 Properties of the nylon-PDMS two-layer phantoms used for the SORS platform validation experiment.

Phantom ID	PDMS layer thickness	TiO_2 concentration	measured diffusion coefficient
a)	500 ± 50 μm	0mg/50ml	0 cm^{-1}
b)	500 ± 50 μm	1mg/50ml	0.3 cm^{-1}
c)	500 ± 50 μm	9mg/50ml	3 cm^{-1}
d)	500 ± 50 μm	90mg/50ml	30 cm^{-1}

5.3.2 SORS measurement on two layer phantoms

Raman spectra were acquired on all four nylon-PDMS optical phantoms. Acquisitions were performed using the SORS platform fitted with fibers having a 400 μm core and 0.5 NA, a laser power of 100 mW at the end of the excitation fiber, an exposure timer of 1 second

per spectrum and 20 spectra per acquisition. The first acquisition on each phantom was performed with no spatial offset ($\Delta s = 0$) and the spatial offset was increased by 50 μm between each acquisition until it reached 1000 μm. All acquired spectra were processed using the workflow presented in Chapter 4. Results for $\Delta s = [0, 200, 600, 1000]$ μm are presented in Figure 5.8.

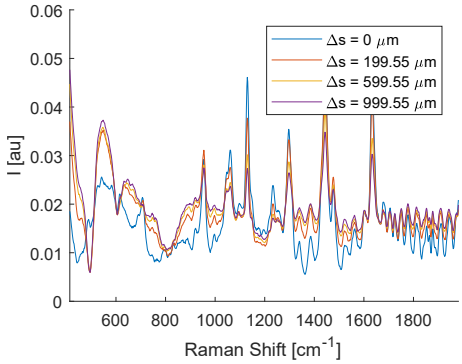

(a) TiO_2 concentration of $0mg/50ml$

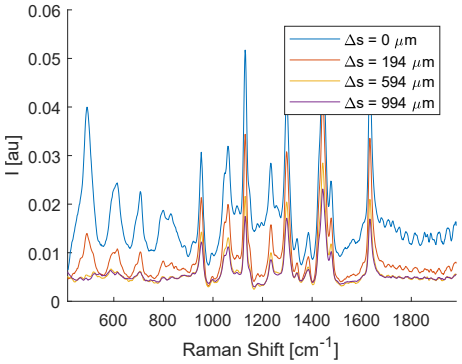

(b) TiO_2 concentration of $1mg/50ml$

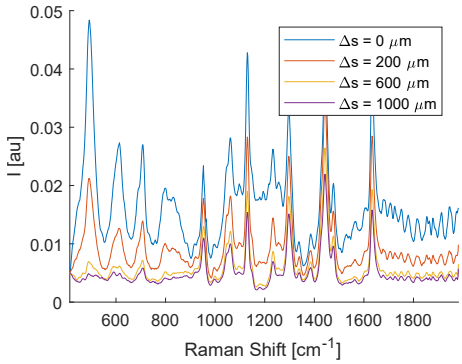

(c) TiO_2 concentration of $9mg/50ml$

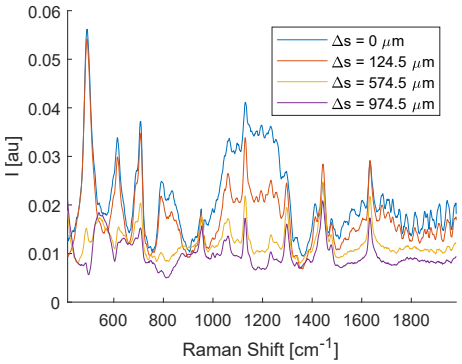

(d) TiO_2 concentration of $90mg/50ml$

Figure 5.8 Processed SORS spectra from Nylon-PDMS phantoms for different concentration of TiO_2 and spatial offsets. The spectral region < 800 cm^{-1} exhibits PDMS peaks whereas the region > 800 cm^{-1} exhibits nylon peaks.

It is interesting to note that the PDMS peaks (< 800 cm^{-1}) are not present in the spectra acquired from phantom (a), even at $\Delta s = 0$. This can be explained by the fact that the scattering coefficient of the PDMS layer of phantom (a) was measured to be zero. Thus, the number of photons undergoing backward Raman scattering to be detected is close to none. It is also interesting to note that the nylon peaks (> 800 cm^{-1}) are much less intense for phantom (d) than for phantom (b) and (c). Because the PDMS layer of phantom (d) has a much larger scattering coefficient, far fewer photons are able to reach the nylon and come back to be detected. However, in order to better analyze the results, it is necessary to look at

the relative intensity loss of each significant PDMS and nylon peaks. To do so, intensities of the three most prominent PDMS peaks and six most prominent nylon peaks were extracted, normalized by their respective value at $\Delta s = 0$ and plotted against Δs. The results are shown in Figure 5.9.

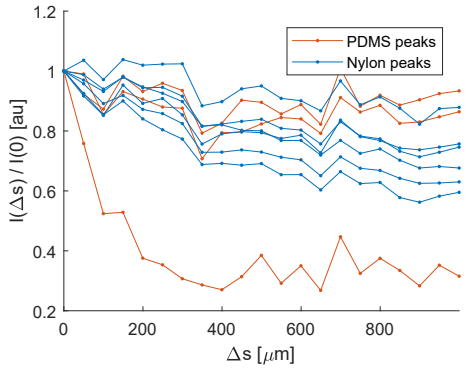

(a) TiO_2 concentration of $0mg/50ml$

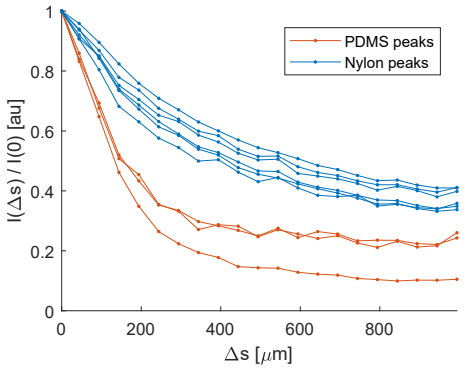

(b) TiO_2 concentration of $1mg/50ml$

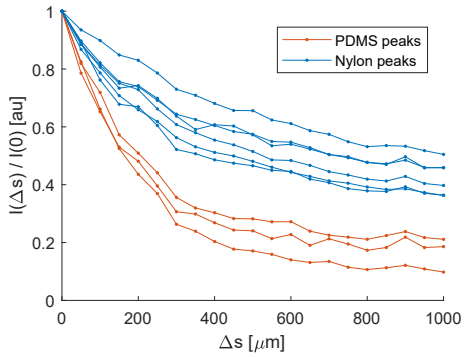

(c) TiO_2 concentration of $9mg/50ml$

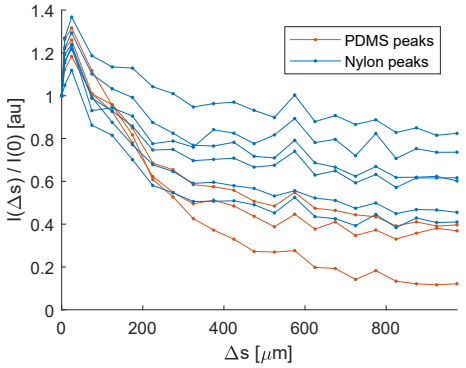

(d) TiO_2 concentration of $90mg/50ml$

Figure 5.9 Variation of the Raman intensity of Nylon and PDMS peaks to increasing spatial offset for different concentration of TiO_2. Each peak intensity has been normalized by its value at $\Delta s = 0$.

As the spatial offset increases, the intensity of both the PDMS and nylon signal decreases. However, for phantom (b) and phantom (c), the intensity from the PDMS falls off quicker than the intensity from the nylon. This trend does not seem to apply for phantom (a) and (d) which indicates that the usability of SORS is limited to samples within a specific range of optical properties. To find out what is the optimal spatial offset for phantoms (b) and (c), the SORS ratio defined in Chapter 2 has been plotted in Figure 5.10. For both phantoms (b) and (c), the SORS ratio increases with Δs, reaching a maximum at $\Delta s = 500$ μm and $\Delta s = 800$ μm respectively. However, since the SNR of the acquired spectra decreases with the spatial offset, $\Delta s = 350$ μm and $\Delta s = 450$ μm might constitute better compromises

between the SORS ratio and the SNR for a SORS probe designed for phantom (b) and (c). Unfortunately, more experimental results are required before a statement can be made about a possible relation between the optimal spatial offset and the optical properties of the tissue.

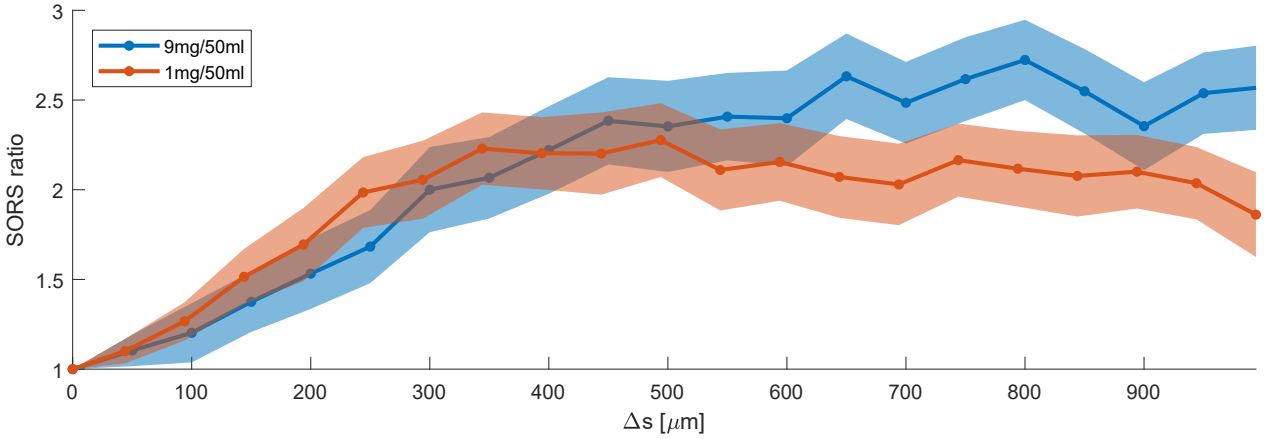

Figure 5.10 Variation of the SORS ratio to increasing spatial offset for Nylon-PDMS phantoms. The error shadows are the sum between the standard deviation for the PDMS peaks and the Nylon peaks.

As for the validation of the SORS platform, the results presented in this chapter indicate that the platform fulfilled all the requirements. The SORS platform is compatible with the LRO Raman system presented in Chapter 3, the fibers can be replaced easily, the platform's maximum spatial offset is 100 mm, the spatial offset increment is 500 nm and the on-axis accuracy is ± 5.0 μm.

CHAPTER 6 CONCLUSION AND RECOMMENDATIONS

This research project conducted within the Laboratory of Radiological Optics (LRO) had as an end goal the construction of a SORS testing and characterization platform. To achieve this goal, the LRO Raman acquisition system and the Raman processing and classification toolbox needed to be upgraded beforehand.

First, the LRO Raman acquisition system was overhauled. Three improved Arduino based laser controllers were built, programmed and tested and a new acquisition system control software was programmed from scratch and named *TimByte*. Final system improvements include: *i*) a faster acquisition time (up to 3× faster for typical acquisitions), *ii*) a precise and stable laser power control, *iii*) an optional automatic exposure algorithm and *iv*) a real-time spectra processing and display panel.

Second, the LRO Raman processing and classification toolboxes were redesigned and the existing Raman processing workflow was modified. A new original cosmic ray removal algorithm was implemented. Two automatic autofluorescence removal algorithms from the literature were implemented and tested, the ModPoly algorithm was determined to be better suited for real-time signal processing due to a faster computing time. A new normalization procedure based on spectrum acquisition parameters was implemented and could serve as a stepping stone for the development of absolute scale Raman spectra analysis. Ultimately, a new classification model training workflow was developed and implemented as part of *ZenClass* (the new LRO classifier training graphical user interface).

Finally, a SORS testing and characterization platform was built and tested. Based on *Thorlabs DDSM100/M* linear translation stage, the SORS platform allows for precise fiber offset control (± 5.0 μm) over a 100 mm range. Custom fiber holders were designed and 3D printed to allow easy replacement of the *bare* optical fibers. The SORS platform was then validated on different custom made two-layer nylon-PDMS optical phantoms. Inline with the literature, results showed that the SORS ratio increases with spatial offset. It was also possible to observe that the optimal spatial offset changed depending on the phantom's top layer diffusion coefficient.

In short, the three main objectives of the project have been achieved and two of the three hypotheses have been answered. It was possible to improve the acquisition time and generally improve the quality of the acquired spectra by optimizing the LRO raman acquisition system and it was possible to improve classification performance, test generalization of trained models and offer better visualization tools by upgrading the LRO Raman processing and

classification toolboxes. However, it was not possible to use the SORS characterization platform to determine the optimal fiber offset for the recovery of the Raman signature from the bottom layer for all tested optical phantoms. Difficulties were met when performing SORS acquisitions on phantoms with non diffusive and high diffusive top layers indicating that the usability of SORS is limited to samples within a range of optical properties.

6.1 Further research

The original motivation behind the SORS characterization platform was to investigate the impact of the spacial offset and fiber numerical aperture on Raman signal acquired from biological tissues in order to manufacture application specific SORS probes. In order to achieve this, the SORS experiments presented in this work should be revised. First, a more accurate and reliable procedure for the creation of two-layer optical phantoms is required to achieve the necessary level of control on the optical properties. Second, SORS experiments with optical phantoms should be conducted on a larger number of different optical properties and top layer thicknesses. Finally, SORS experiments on biological tissue may be necessary to validate the results obtained on optical phantoms.

BIBLIOGRAPHY

[1] M. Jermyn, J. Mercier, K. Aubertin, J. Desroches, K. Urmey, J. Karamchandiani, E. Marple, M. C. Guiot, F. Leblond, and K. Petrecca, "Highly accurate detection of cancer in situ with intraoperative, label-free, multimodal optical spectroscopy," *Cancer Research*, vol. 77, no. 14, pp. 3942–3950, 2017.

[2] Canadian Cancer Society, "Canadian Cancer Statistics Special topic : Predictions of the future burden of cancer in Canada," *Public Health Agency of Canada*, pp. 1–151, 2015.

[3] M. Jermyn, J. Desroches, K. Aubertin, K. St-Arnaud, W. J. Madore, E. De Montigny, M. C. Guiot, D. Trudel, B. C. Wilson, K. Petrecca, and F. Leblond, "A review of Raman spectroscopy advances with an emphasis on clinical translation challenges in oncology," *Physics in Medicine and Biology*, vol. 61, no. 23, pp. R370–R400, 2016.

[4] M. Jermyn, K. Mok, J. Mercier, J. Desroches, J. Pichette, K. Saint-Arnaud, L. Bernstein, M. C. Guiot, K. Petrecca, and F. Leblond, "Intraoperative brain cancer detection with Raman spectroscopy in humans," *Science Translational Medicine*, vol. 7, no. 274, pp. 1–10, 2015.

[5] J. Desroches, M. Jermyn, M. Pinto, F. Picot, M. A. Tremblay, S. Obaid, E. Marple, K. Urmey, D. Trudel, G. Soulez, M. C. Guiot, B. C. Wilson, K. Petrecca, and F. Leblond, "A new method using Raman spectroscopy for in vivo targeted brain cancer tissue biopsy," *Scientific Reports*, vol. 8, no. 1, pp. 1–10, 2018.

[6] S. P. Singh, A. Deshmukh, P. Chaturvedi, and C. Murali Krishna, "In vivo Raman spectroscopic identification of premalignant lesions in oral buccal mucosa," *Journal of Biomedical Optics*, vol. 17, p. 1050021, oct 2012.

[7] B. Li, Z.-Y. Gu, K.-X. Yan, Z.-N. Wen, Z.-H. Zhao, L.-J. Li, and Y. Li, "Evaluating oral epithelial dysplasia classification system by near-infrared Raman spectroscopy," *Oncotarget*, vol. 8, no. 44, pp. 76257–76265, 2017.

[8] P. Matousek, I. P. Clark, E. R. C. Draper, M. D. Morris, a. E. Goodship, N. Everall, M. Towrie, W. F. Finney, and a. W. Parker, "accelerated paper Subsurface Probing in Diffusely Scattering Media Using Spatially Offset Raman Spectroscopy," *Applied Spectroscopy*, vol. 59, no. 4, pp. 393–400, 2005.

[9] P. Matousek, M. D. Morris, N. Everall, I. P. Clark, M. Towrie, E. Draper, A. Goodship, and A. W. Parker, "Numerical simulations of subsurface probing in diffusely scattering media using spatially offset Raman spectroscopy," *Applied Spectroscopy*, vol. 59, no. 12, pp. 1485–1492, 2005.

[10] P. Matousek, E. R. C. Draper, A. E. Goodship, I. P. Clark, K. L. Ronayne, and A. W. Parker, "Non-invasive Raman spectroscopy of human tissue in vivo," *Central Laser Facility Annual Report*, pp. 133–135, 2006.

[11] N. Stone, R. Baker, K. Rogers, A. W. Parker, and P. Matousek, "Subsurface probing of calcifications with spatially offset Raman spectroscopy (SORS): future possibilities for the diagnosis of breast cancer.," *The Analyst*, vol. 132, no. 9, pp. 899–905, 2007.

[12] P. Matousek, "Deep non-invasive Raman spectroscopy of living tissue and powders.," *Chemical Society reviews*, vol. 36, no. 8, pp. 1292–1304, 2007.

[13] M. V. Schulmerich, J. H. Cole, K. a. Dooley, M. D. Morris, J. M. Kreider, S. a. Goldstein, S. Srinivasan, and B. W. Pogue, "Noninvasive Raman tomographic imaging of canine bone tissue," *Journal of Biomedical Optics*, vol. 13, no. 2, p. 020506, 2008.

[14] P. Matousek and N. Stone, "Recent advances in the development of Raman spectroscopy for deep non-invasive medical diagnosis," *Journal of Biophotonics*, vol. 6, pp. 7–19, jan 2013.

[15] Z. Wang, H. Ding, G. Lu, and X. Bi, "Use of a mechanical iris-based fiber optic probe for spatially offset Raman spectroscopy.," *Optics letters*, vol. 39, no. 13, pp. 3790–3, 2014.

[16] P. Matousek and N. Stone, "Development of deep subsurface Raman spectroscopy for medical diagnosis and disease monitoring," *Chem. Soc. Rev.*, vol. 45, pp. 1794–1802, 2015.

[17] M. D. Keller, E. Vargis, N. de Matos Granja, R. H. Wilson, M. Mycek, M. C. Kelley, and A. Mahadevan-Jansen, "Development of a spatially offset Raman spectroscopy probe for breast tumor surgical margin evaluation.," *Journal of biomedical optics*, vol. 16, no. 7, p. 077006, 2011.

[18] C. V. Raman, "A change of wave-length in light scattering [8]," 1928.

[19] S. O. Williams and D. G. Imre, "Raman spectroscopy: time-dependent pictures," *The Journal of Physical Chemistry*, vol. 92, pp. 3363–3374, jun 1988.

[20] E. Smith and G. Dent, "Modern Raman Spectrocopy: A Practical Approach," *Spectroscopy*, vol. 5, pp. 1–210, 2005.

[21] C. A. F. De Oliveira Penido, M. T. T. Pacheco, I. K. Lednev, and L. Silveira, "Raman spectroscopy in forensic analysis: Identification of cocaine and other illegal drugs of abuse," *Journal of Raman Spectroscopy*, vol. 47, no. 1, pp. 28–38, 2016.

[22] J. Jehlička and H. G. Edwards, "Raman spectroscopy as a tool for the non-destructive identification of organic minerals in the geological record," *Organic Geochemistry*, vol. 39, no. 4, pp. 371–386, 2008.

[23] S. Wartewig and R. H. Neubert, "Pharmaceutical applications of Mid-IR and Raman spectroscopy," *Advanced Drug Delivery Reviews*, vol. 57, no. 8, pp. 1144–1170, 2005.

[24] W. Kiefer, A. Mazzolini, and P. Stoddart, "Recent Advances in linear and nonlinear Raman spectroscopy I," *Journal of Raman Spectroscopy*, vol. 38, no. April, pp. 1538–1553, 2007.

[25] J. Wu, M. S. Feld, M. G. Müller, I. Georgakoudi, and Q. Zhang, "Intrinsic fluorescence spectroscopy in turbid media: disentangling effects of scattering and absorption," *Appl. Opt.*, vol. 40, no. 25, pp. 4633–4646, 2001.

[26] M. A. Veenstra, O. Palyvoda, H. Alahwal, M. Jovanovski, L. A. Reisner, B. King, J. Poulik, and M. D. Klein, "Raman spectroscopy in the diagnosis of ulcerative colitis," *European Journal of Pediatric Surgery*, vol. 25, no. 1, pp. 56–59, 2015.

[27] S. Sigurdsson, P. A. Philipsen, L. K. Hansen, J. Larsen, M. Gniadecka, and H. C. Wulf, "Detection of skin cancer by classification of Raman spectra," *IEEE Trans Biomed Eng*, vol. 51, no. 10, pp. 1784–1793, 2004.

[28] Q. Li, W. Li, J. Zhang, and Z. Xu, "An improved k -nearest neighbour method to diagnose breast cancer," *The Analyst*, 2018.

[29] S. K. Teh, W. Zheng, K. Y. Ho, M. Teh, K. G. Yeoh, and Z. Huang, "Diagnostic potential of near-infrared Raman spectroscopy in the stomach: Differentiating dysplasia from normal tissue," *British Journal of Cancer*, vol. 98, no. 2, pp. 457–465, 2008.

[30] C.-w. Hsu, C.-c. Huang, J.-h. Sheu, C.-w. Lin, and L.-f. Lin, "Novel Method for Differentiating Histological Types of Gastric Adenocarcinoma by Using Confocal Raman Microspectroscopy," pp. 1–12, 2016.

[31] T. Kawabata, T. Mizuno, S. Okazaki, M. Hiramatsu, T. Setoguchi, H. Kikuchi, M. Yamamoto, Y. Hiramatsu, K. Kondo, M. Baba, M. Ohta, K. Kamiya, T. Tanaka, S. Suzuki, and H. Konno, "Optical diagnosis of gastric cancer using near-infrared multichannel Raman spectroscopy with a 1064-nm excitation wavelength," *Journal of Gastroenterology*, vol. 43, no. 4, pp. 283–290, 2008.

[32] M. Tang, L. Xia, D. Wei, S. Yan, C. Du, and H.-L. Cui, "Distinguishing Different Cancerous Human Cells by Raman Spectroscopy Based on Discriminant Analysis Methods," *Applied Sciences*, vol. 7, no. 9, p. 900, 2017.

[33] M. Sattlecker, C. Bessant, J. Smith, and N. Stone, "Investigation of support vector machines and Raman spectroscopy for lymph node diagnostics," *The Analyst*, vol. 135, no. 5, p. 895, 2010.

[34] B. E. Boser, I. M. Guyon, and V. N. Vapnik, "A training algorithm for optimal margin classifiers," *Proceedings of the fifth annual workshop on Computational learning theory - COLT '92*, pp. 144–152, 1992.

[35] K. Hajian-Tilaki, "Receiver Operating Characteristic (ROC) Curve Analysis for Medical Diagnostic Test Evaluation.," *Caspian journal of internal medicine*, vol. 4, no. 2, pp. 627–35, 2013.

[36] *Atomic And Nuclear Physics*. Pearson Education India, 2008.

[37] S. J. Choquette, E. S. Etz, W. S. Hurst, D. H. Blackburn, and S. D. Leigh, "Relative Intensity Correction of Raman Spectrometers: NIST SRMs 2241 through 2243 for 785 nm, 532 nm, and 488 nm/514.5 nm Excitation," *Applied Spectroscopy*, vol. 61, pp. 117–129, feb 2007.

[38] A. R. Radzol, K. Y. Lee, W. Mansor, and A. Azman, "Optimization of Savitzky-Golay smoothing filter for salivary surface enhanced Raman spectra of non structural protein 1," *IEEE Region 10 Annual International Conference, Proceedings/TENCON*, vol. 2015-January, pp. 9–14, 2015.

[39] N. Kumar, K. Alam, and A. H. Siddiqi, "vitzk y – Gola y and W a v elet T r ansf or m Savitzk vitzky – Gola y – Golay ansfor orm Based Rama Spectroscopic data Denoising," vol. 9, no. 21, pp. 297–305, 2016.

[40] J. Zhao, H. Lui, D. I. Mclean, and H. Zeng, "Automated autofluorescence background subtraction algorithm for biomedical raman spectroscopy," *Applied Spectroscopy*, vol. 61, no. 11, pp. 1225–1232, 2007.

[41] F. Ayers, A. Grant, D. Kuo, D. J. Cuccia, and A. J. Durkin, "Fabrication and characterization of silicone-based tissue phantoms with tunable optical properties in the visible and near infrared domain," vol. 6870, p. 687007, 2008.

[42] G. J. Greening, R. Istfan, L. M. Higgins, K. Balachandran, D. Roblyer, M. C. Pierce, and T. J. Muldoon, "Characterization of thin poly(dimethylsiloxane)-based tissue-simulating phantoms with tunable reduced scattering and absorption coefficients at visible and near-infrared wavelengths," *Journal of Biomedical Optics*, vol. 19, no. 11, p. 115002, 2014.

[43] G. J. Greening, H. M. James, and T. J. Muldoon, *Optical Phantoms: Diffuse and Sub-diffuse Imaging and Spectroscopy Validation*. SPIE, 2015.

APPENDIX A IPS LASER CONTROLLER SCHEMATIC

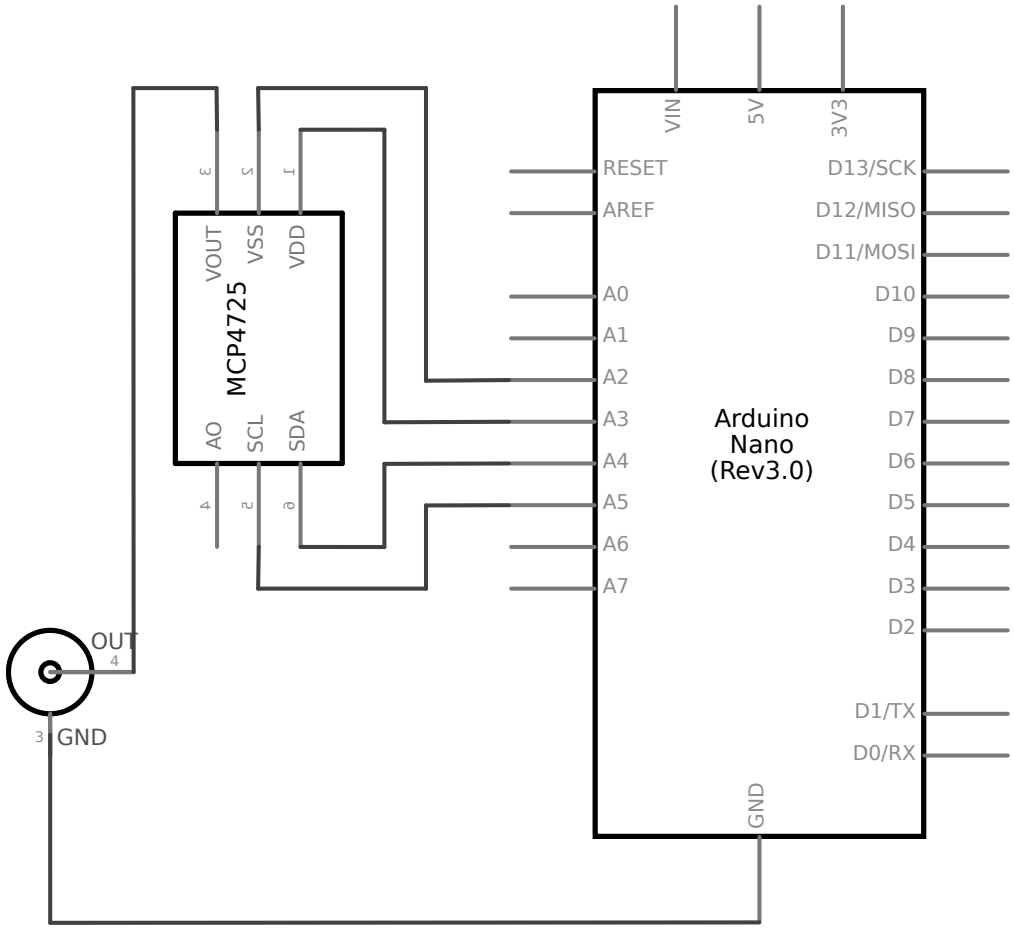

APPENDIX B LASER QUANTUM LASER CONTROLLER SCHEMATIC